

## Chinese Society of Aeronautics and Astronautics & Beihang University

#### **Chinese Journal of Aeronautics**

cja@buaa.edu.cn www.sciencedirect.com



#### **FULL LENGTH ARTICLE**

# Grouping-sparsity enforcing LASSO-based outlier detection and correction for Doppler velocity determination in urban areas <sup>☆</sup>



Zhen GAO a, Rong YANG a,\*, Xingqun ZHAN a, Yiping JIANG b

Received 24 June 2024; revised 13 August 2024; accepted 18 January 2025 Available online 1 March 2025

#### KEYWORDS

Global Navigation Satellite System (GNSS); Velocity estimation; Doppler measurements; Sparse estimation; Urban area Abstract Velocity incorporates user dynamic characteristics, facilitating more precise predictions about the positioning. However, the positioning, velocity, and timing services derived from Global Navigation Satellite System (GNSS) undergo accuracy degradation in urban environments due to multipath/Non-Line of Sight (NLOS) effects. Fault detection and exclusion (FDE) methods can mitigate these effects. However, the existing methods, such as the multi-hypothesis separation solution (MHSS), exhibit high computational burdens and cannot perform accurate exclusion due to the excessive fault modes. In response, a fault detection and correction (FDC) method is developed to address outliers arising from multipath/NLOS in the Doppler measurements. To alleviate computational demands while simultaneously improving velocity estimation accuracy, multipath/NLOS sparsity assumptions and grouping constraints are introduced. Specifically, the grouping-sparsity enforcing Least Absolute Shrinkage and Selection Operator (GS-LASSO) is introduced to jointly detect and correct multipath/NLOS-induced outliers. A grouping strategy based on sky-map and carrier-to-noise ratio is introduced, which is coupled with a new cost function to improve sparsity estimation. To facilitate the implementation, a solver and parameter-tuning method incorporating false alarm rates are developed. The performance of GS-LASSO is compared with that of MHSS.

E-mail address: rongyang@sjtu.edu.cn (R. YANG).

<sup>\*</sup> This article is part of a special issue entitled: 'GNSS Technology and Application' published in Chinese Journal of Aeronautics. Peer review under responsibility of Editorial Committee of CJA



Production and hosting by Elsevier

<sup>&</sup>lt;sup>a</sup> School of Aeronautics and Astronautics, Shanghai Jiao Tong University, Shanghai 200240, China

<sup>&</sup>lt;sup>b</sup> Department of Aeronautical and Aviation Engineering, Hong Kong Polytechnic University 999077, Hong Kong, China

<sup>\*</sup> Corresponding author.

The results show that GS-LASSO reduces greater velocity errors in the urban environment, while requiring limited computational load.

© 2025 The Author(s). Published by Elsevier Ltd on behalf of Chinese Society of Aeronautics and Astronautics. This is an open access article under the CC BY-NC-ND license (http://creativecommons.org/licenses/by-nc-nd/4.0/).

#### 1. Introduction

Thanks to the advancement of smart cities and intelligent transportation, the Global Navigation Satellite System (GNSS) is receiving increasing attention for its capability to provide high-precision position, velocity, and time (PVT) solutions.<sup>1,2</sup> However, in urban environments, the accuracy of PVT solutions is often compromised due to multipath/NLOS effects. Velocity, which measures changes in user dynamics, is crucial for ensuring accurate positioning. Inaccuracies in velocity estimation can lead to degraded performance in positioning prediction. Additionally, velocity information can serve as prior information for GNSS or other sensors, enhancing various PVT applications. Research has shown that velocity-related information is beneficial in navigation tasks such as GNSS integrity monitoring, 4 GNSS-based positioning, 5,6 stereo visual odometry localization, and initial alignment of Inertial Navigation Systems (INS).8 Thus, providing high-precision GNSS velocity information in urban environments is vital.

For a stand-alone GNSS receiver, velocity can be estimated using various measurements. Time-difference pseudorange, time-difference carrier-phase, and Doppler measurements are commonly employed. Among these, time-difference pseudorange provides the lowest accuracy, making it impractical for certain applications. Time-difference carrier-phase can theoretically provide the highest accuracy, up to centimeter-persecond, but the frequent occurrence of cycle slips disrupts the continuity of the carrier phase, resulting in low availability. Doppler measurements are the most robust, offering decimeter-per-second accuracy. Furthermore, some studies combined these measurements to compensate for their respective drawbacks. 10-12 However, all these measurements are optimized for users in open-sky environments. In urban areas, multipath/NLOS effects are significant and can simultaneously impact multiple satellites, causing the velocity accuracy obtained from original measurements to occasionally fall short of expectations.

Several studies have been conducted to address challenges in urban environments regarding velocity determination. Sparse kernel learning<sup>13</sup> and Tikhonov regularized kernel learning<sup>14</sup> were utilized to enhance velocity determination accuracy. However, the false alarm rate is not fully considered in such kernel learning methods. These methods may provide surplus correction information in the fault-free case. Auxiliary information from the ray tracing was also harnessed to improve velocity measurement accuracy. 15 Another common approach is fault detection and exclusion (FDE), which involves detecting whether metrics associated with multipath are statistically greater than predefined thresholds and excluding satellites contaminated by multipath/NLOS. For singlesatellite faults, the chi-square test was employed to eliminate multipath/NLOS in Doppler and time-difference carrierphase measurements. 16 For multi-satellite faults in urban

areas. Guo et al. employed the Random Sample Consensus (RANSAC) method to estimate velocity estimation with a prior dynamic model.<sup>17</sup> The multi-hypothesis separation solution (MHSS) has also been utilized to conduct FDE on timedifference carrier-phase measurements, particularly in rail and road applications. 18 Gao et al. extended MHSS to accommodate various measurements, including time-difference pseutime-difference carrier-phase, and Doppler measurements. 19 However, in urban environments, the presence of multi-fault modes leads to high computational complexity for MHSS in practical applications. The real-time computational burden of MHSS requires further evaluation. To ensure the effectiveness of MHSS algorithm, it might be necessary to compromise part of its exclusion performance. Additionally, several issues have not been fully addressed, necessitating theoretical optimization. For one thing, the spatial correlation of multipath/NLOS in urban environments has not been adequately considered. For another thing, some scholars have observed that only a fraction of satellites may be affected by multipath/NLOS in urban environments. Based on the sparse estimation, the standard LASSO, <sup>20</sup> Elastic Net, <sup>2</sup> and re-weighted L1 regularization<sup>22</sup> were employed to detect the multipath/NLOS and optimize pseudorange-based positioning. However, this hypothesis is not fully considered in the existing work on velocity determination. Thus, a research gap exists in improving the accuracy of velocity measurement in urban environments.

Inspired by FDE, a fault detection and correction (FDC) strategy for velocity estimation in urban environments is adopted. Rather than excluding satellites contaminated by multipath/NLOS, correcting the outliers introduced by multipath/NLOS in the measurements is the focus. To facilitate this approach, two key assumptions are introduced. The first assumption, referred to as multipath/NLOS sparsity, 20 suggests that only a small fraction of GNSS measurements is affected by multipath/NLOS interference. The second assumption, known as fault or multipath/NLOS grouping.<sup>23</sup> shows that satellites with similar geometric distributions are often affected collectively due to spatial correlation. This correlation stems from the tendency of signals emitted by satellites with similar elevation and azimuth angles to reflect from the same reflector, thereby producing correlated signals. Additionally, Carrier-to-Noise Density  $(C/N_0)$ , which reflects the extent of signal fading and characterizes the impact of multipath/ NLOS,<sup>24</sup> needs to be considered. Fig. 1 visually illustrates these two assumptions through a map of multi-system satellites. Satellites of the same group are marked by the same color. Diamond, circle, and star shapes denote the constellations for the three satellite systems (GAL, BDS, GPS). The satellites of black and red groups are obscured, indicating that the Doppler signals may contain outliers. According to our assumptions, only a small fraction of satellites is subject to multipath/NLOS contamination, and multipath/NLOS tends to exhibit grouping behavior based on geometric conditions.

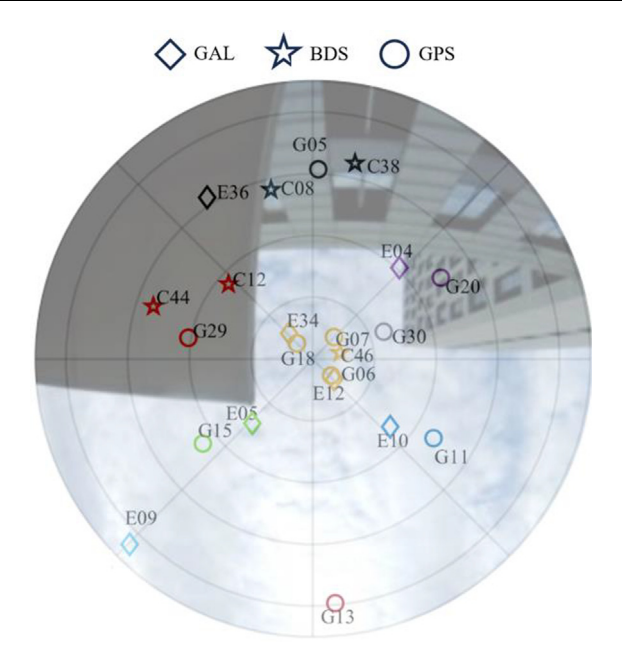


**Fig. 1** An illustrative example of a multi-constellation map with sparsity hypothesis and grouping hypothesis.

Based on the above assumptions, a grouping-sparsity enforcing Least Absolute Shrinkage and Selection Operator (LASSO) algorithm named GS-LASSO is proposed. The GS-LASSO is customized for achieving Fault Detection and Correction (FDC) to enhance Doppler velocity accuracy in the measurement domain. LASSO is recognized as a linear estimator for regression problems with sparsity assumptions.<sup>25</sup> By incorporating a sparsity-encouraging cost function on the standard least squares, LASSO allows for joint detection and amplitude estimation. The applicability of LASSO in the GNSS domain has been validated, including cases of singlepoint positioning,<sup>20</sup> GNSS spoofing detection,<sup>26</sup> cooperative navigation,<sup>27</sup> and integrity monitoring.<sup>28</sup> LASSO, with the sparsity assumption, enables users to focus on the limited satellites potentially affected by multipath/NLOS, thereby reducing computational load. Building on the grouping assumption, the spatial correlation of multipath/NLOS is further considered, and LASSO is extended to GS-LASSO. Grouping constraints allow satellites likely affected by the same source to be simultaneously considered, thereby improving estimation accuracy. By solving GS-LASSO, whether multipath/NLOS effects are present can be determined. Then, outliers in Doppler measurements can be synchronously estimated and corrected. Therefore, FDC can be performed to obtain optimized velocity solutions. GS-LASSO is compared with MHSS<sup>19</sup> using data from urban environments to validate effectiveness in terms of accuracy and computation time.

Our technical contributions can be summarized as follows.

(1) Skyplot-assisted multipath/NLOS grouping for grouping constraints. Satellites are grouped based on elevation and azimuth angles provided by the skyplot. Additionally, C/N<sub>0</sub> is considered as input for multipath/NLOS grouping. By incorporating grouped constraints, the LASSO model is enhanced to a group LASSO model,

- which attenuates the influence of unimportant groups to zero while preserving information from groups containing faulty satellites.
- (2) New cost function to ensure sparsity and estimation accuracy. The estimation of a generic group LASSO with traditional cost functions is prone to outliers and has limited sparsity-holding capabilities. In response, we introduce an inverse tangent cost function (arctangent cost) to improve the sparsity of the estimation results and enhance the accuracy of fault magnitude estimation. Consequently, the GS-LASSO model with arctangent cost is developed.
- (3) Efficient solver design for GS-LASSO. A closed-form solution is absent for all LASSO-related problems. To facilitate GS-LASSO, a solver for numerical solutions is developed. Comprehensive steps with analysis are outlined to ensure that the estimation results converge to the global optimum. Furthermore, computation time is examined using complexity analysis and real data to demonstrate the superiority of the GS-LASSO.
- (4) Performance analysis of GS-LASSO covering false alarm rate and detection ability. Aside from the accuracy, false alarm rate and detection ability are also considered. A parameter tuning criterion is proposed to ensure the correction information is provided below the false alarm rate in fault-free cases. A sufficient condition for multipath/NLOS detection is also provided.

The structure of the remaining paper is as follows. In Section 2, the preliminary knowledge regarding the Doppler velocity and the LASSO is introduced. In Section 3, the GS-LASSO model establishment and solver design are presented. In Section 4, the performance of the proposed GS-LASSO regarding the false alarm rate and detection ability is examined. In Section 5, experimental results are analyzed. Section 6 summarizes the paper.

## 2. Mathematics model for Doppler-based velocity determination and LASSO-enforcing FDC

In this section, the mathematical model for the Doppler velocity determination is first presented, followed by the analysis of the multipath/NLOS on the velocity estimation. Subsequently, a constrained combinatorial optimization problem, analogous to LASSO, is introduced for modelling the multipath/NLOS sparsity.

#### 2.1. Doppler-based velocity determination method

The frequency of the GNSS carrier signal received by the receiver differs from the frequency of the carrier signal transmitted by the satellite according to the Doppler effect. This occurs when there is relative motion between the GNSS receiver and the satellite. The difference in frequency is referred to as the Doppler frequency shift. The Doppler effect can be described as<sup>29</sup>

$$f_{\rm d} = f_{\rm r} - f^{\rm s} \tag{1}$$

where  $f^s$  is the signal frequency transmitted by the satellite.  $f_r$  is the signal frequency received by the receiver.  $f_d$  is the Doppler frequency shift. The magnitude of the Doppler

frequency shift is related with the change rate of ranges between receivers and satellites. If  $\dot{\rho}$  is the change rate and c is the speed of light, Eq. (2) holds as

$$\dot{\rho} = -\frac{c}{f^s} f_{\rm d} = -\frac{c}{f^s} (f_{\rm r} - f^s) \tag{2}$$

The Doppler frequency shift  $f_{\rm d}$  can be directly obtained by the GNSS receiver. The velocity derived from the raw Doppler frequency shift generated by the receiver is the instantaneous one. The GNSS single-point positioning yields the Doppler velocity determination mathematical formulations. Differentiating the pseudorange concerning time introduces the following equation

$$\dot{\rho}_{j} = \frac{\mathbf{r}_{r} - \mathbf{r}^{s}}{\rho_{j}} (\dot{\mathbf{r}}_{r} - \dot{\mathbf{r}}^{s}) + c \left(\dot{d}_{rc} - \dot{d}_{sc}^{j}\right) + \dot{d}_{trop}^{j} + \dot{d}_{ion}^{j} + \dot{d}_{mp}^{j} + \dot{\varepsilon}^{j}$$

$$(3)$$

where the symbol  $\cdot$  is the inner product between two vectors.  $\rho_i$ is the pseudorange between jth satellite and receivers.  $\dot{\rho}_i$  is the change rate of pseudorange between the jth satellite and receivers, which can be calculated from Eq. (2).  $\dot{d}_{\rm ion}^{j}$  and  $\dot{d}_{\rm trop}^{j}$  are the jth change rate of the ionospheric and tropospheric delay, respectively.  $\dot{d}_{MP/NLOS}^{J}$  are errors caused by the multipath/ NLOS.  $r_{\rm r}$  and  $\dot{r}_{\rm r}$  denote the position and velocity vectors of the receiver, respectively.  $r^s$  and  $\dot{r}^s$  represent the position and velocity vectors of the satellite, respectively.  $\dot{d}_{\rm cr}$  and  $\dot{d}_{\rm cs}^{j}$  denote the clock drifts of the receiver and the *j*th satellite, respectively.  $\dot{\varepsilon}^{j}$  signifies the noise rate. Satellite velocity and the clock speed can both be directly obtained from navigation messages. Since the time intervals for velocity measurements are typically tiny in practical calculations, the variations in ionospheric and tropospheric delays can be neglected. Eq. (3) involves only four unknowns, including the three-dimensional velocity of the receiver and its clock drift. Therefore, theoretically, if  $n(n \ge 4)$  satellites can be in view, aforementioned unknowns can be reformulated as the following form as Eq. (4) with the elements listed from Eqs. (5)–(7).

$$Z = HX + \dot{d}_{\text{MP/NLOS}} + \dot{\varepsilon} \tag{4}$$

$$X = \begin{bmatrix} v_x \\ v_y \\ v_z \\ c\dot{d}_{cr} \end{bmatrix}$$
 (5)

$$\boldsymbol{H} = \begin{bmatrix} -e_1^x & -e_1^y & -e_1^z & 1\\ -e_2^x & -e_2^y & -e_2^z & 1\\ \vdots & \vdots & \vdots & \vdots\\ -e_1^x & -e_2^y & -e_2^z & 1 \end{bmatrix}$$
(6)

$$Z = \frac{\mathbf{r}_{\mathrm{r}} - \mathbf{r}^{\mathrm{s}}}{\rho} \dot{\mathbf{r}}^{\mathrm{s}} + c \dot{\mathbf{d}}_{\mathrm{t}} - \dot{\rho} \tag{7}$$

where Z is the Doppler observation.X is the state to be estimated containing the three dimension velocity and clock drifts.  $e_j^x$ ,  $e_j^y$  and  $e_j^z$  are the elements of the three-dimensional line-of-sight unit vector. H is the design matrix. Since the distance between GNSS satellites and the earth is large,  $e_j^x$ ,  $e_j^y$  and  $e_j^z$  do not change a lot for receivers within a hundred meters.

Therefore, estimation result from the single-point positioning can be used to provide H matrix. Note that the  $\dot{\epsilon}$  in Eq. (4) does not follow a standard Gaussian distribution. To simplify subsequent expressions, Eq. (4) are first normalized by the standard deviation to make each element of  $\dot{\epsilon}$  follow a standard Gaussian distribution.

 $d_{\text{MP/NLOS}}$  is small in the open-sky environment. However, in the urban area, the multipath/NLOS is significant. On the one hand,  $\dot{d}_{\rm MP/NLOS}$  will become large due to the rapid change of the multipath/NLOS. On the other hand, the Doppler shift is determined by the combined velocities of the wave source and user, projected onto the line connecting them and aligned with the wave propagation direction. However, Doppler measurements are also highly affected by NLOS and multipath due to the tall building. NLOS refers to situations where the direct signal is blocked, and only reflected signals reach the receiver. 30 Multipath typically refers to scenarios where both direct and reflected signals are received simultaneously. Although the mechanisms underlying these two phenomena are different, both NLOS and multipath effects change the direction of wave propagation and introduce errors in the Doppler shift received by the receiver, impacting the accuracy of velocity estimation based on Doppler shift. Some literature defaults to modeling both outliers caused by NLOS and multipath as an additive fault in Doppler measurements. 17,19 We follow this assumption and provide a preliminary analysis of its feasibility in Appendix A. By rearranging the above equations, the model is

$$Z = HX + f + \epsilon \tag{8}$$

where f includes the outliers caused by the change rate and the Doppler frequency shift. Note that we model the effects of NLOS and multipath on Doppler measurements similarly. Impacts of both NLOS and multipath on Doppler are taken as outliers. This study does not necessarily make a distinction between the two error sources.  $\epsilon = \dot{\epsilon}$  denotes the noise. After getting the approximate position and the design matrix H, the estimated velocity can be estimated using the least square (LS) as

$$X = (\mathbf{H}^{\mathrm{T}}\mathbf{H})^{-1}\mathbf{H}^{\mathrm{T}}(\mathbf{Z} - \mathbf{f})$$
(9)

When multipath/NLOS is present, the estimation from Eq. (9) deviates significantly from the ground truth. To mitigate the impact of multipath/NLOS, an effective approach is to detect the existence of f and then correct it in Eq. (9).

#### 2.2. LASSO-aware multipath/NLOS detection and correction

A commonly employed technique for identifying faults in GNSS measurements involves the receiver autonomous integrity monitoring (RAIM).<sup>31</sup> The sum of squares for errors (SSE) is as follows if the multipath/NLOS exists

SSE = 
$$(\mathbf{Z} - \mathbf{f})^{\mathrm{T}} \Big( \mathbf{I} - \mathbf{H} \Big( \mathbf{H}^{\mathrm{T}} \mathbf{H} \Big)^{-1} \mathbf{H}^{\mathrm{T}} \Big) (\mathbf{Z} - \mathbf{f})$$
  
=  $(\mathbf{Z} - \mathbf{f})^{\mathrm{T}} \mathbf{W} (\mathbf{Z} - \mathbf{f})$  (10)

where  $W = I - H(H^TH)^{-1}H^T$  is an idempotent matrix satisfying  $W^TW = W$ . If we hope to estimate f, an obvious method is to solve the optimization problem formulated in Eq. (10). We find f to minimize SSE/2:

$$\underset{f}{\operatorname{argmin}} \frac{1}{2} (\boldsymbol{Z} - \boldsymbol{f})^{\mathsf{T}} \boldsymbol{W} (\boldsymbol{Z} - \boldsymbol{f}) \tag{11}$$

If complete information regarding potential multipath/ NLOS is available, the solutions of Eq. (11) can be attained through exhaustive exploration using MHSS to try all feasible solutions. However, users are often unaware of which satellites are affected, significantly complicating the process of RAIM. This issue becomes particularly challenging when multiple multipath/NLOS occurs simultaneously. Therefore, this method is complicated in practice.

To solve this, we hold that constraining the number of multipath/NLOS is imperative to yield a meaningful solution. This constraint is feasible because, in urban scenarios, simultaneous multipath/NLOS in all satellites is rare. Instead, a subset of satellites typically exhibits dominant effect by the multipath/NLOS. Under this assumption, we assume multipath/NLOS in different GNSS signal channels are usually sparse in nature. A new constraint is added and Eq. (11) is reformulated as

$$\underset{f}{\operatorname{argmin}} \frac{1}{2} (\boldsymbol{Z} - \boldsymbol{f})^{\mathsf{T}} \boldsymbol{W} (\boldsymbol{Z} - \boldsymbol{f})$$

$$s.t. |\boldsymbol{f}|_{0} \leq \omega$$

$$(12)$$

where  $|f|_0$  is the  $l_0$ -norm and  $\omega$  is a user-specified constant to judge the number of zero elements in f. However, the optimization problem encompassing  $l_0$ -norm is inherently non-convex and non-smooth. Consequently, Eq. (12) is hard to solve. An alternative is to consider the  $l_1$ -norm instead of the  $l_0$ -norm. Therefore, Eq. (13) is considered

$$\underset{f}{\operatorname{argmin}} \frac{1}{2} (\boldsymbol{Z} - \boldsymbol{f})^{\mathsf{T}} \boldsymbol{W} (\boldsymbol{Z} - \boldsymbol{f})$$

$$s.t. |\boldsymbol{f}|_{1} \leq \delta$$
(13)

where  $|f|_1$  is the  $l_1$ -norm and  $\delta$  is a constant given by user. Due to the convex optimization, Eq. (13) can be tackled with superior computational efficiency. Using the Karush-Kuhn-Tucker condition, Eq. (13) can be rewritten as a Lagrange multiplier-driving unconstrained penalized optimization problem

$$\underset{f}{\operatorname{argmin}} \left[ \frac{1}{2} (\boldsymbol{W}(\boldsymbol{Z} - \boldsymbol{f}))^{\mathsf{T}} (\boldsymbol{W}(\boldsymbol{Z} - \boldsymbol{f})) + \lambda |\boldsymbol{f}|_{1} \right]$$
(14)

where  $\lambda > 0$  is the Lagrange multiplier. Eq. (14) shows a  $l_1$ -norm cost (or penalty) is added after the least square. This aligns with the typical LASSO problem. LASSO is a linear regression estimator to get the sparse regression result, widely used in the domain of compressive sensing,  $^{32}$  chemical process  $^{33}$  and mechanical engineering  $^{34}$ . It can result in a shrinkage of the estimated f, forcing some of them to be zero. Therefore, only variables in f that have a significant impact on the regression results will be selected. As a result, LASSO facilitates automatic detection and magnitude estimation. Using the algorithm in Ref. 25, Eq. (14) can be easily solved and f is obtained. After getting f, it can be removed in Eq. (9) and the velocity error is corrected. Hence, a better solution can be expected.

#### 3. GS-LASSO enforcing Doppler velocity determination design

To mitigate the impact of multipath/NLOS on Doppler velocity determination, a GS-LASSO approach, derived from LASSO, is proposed for urban environments. GS-LASSO is based on assumptions of multipath/NLOS sparsity and group-

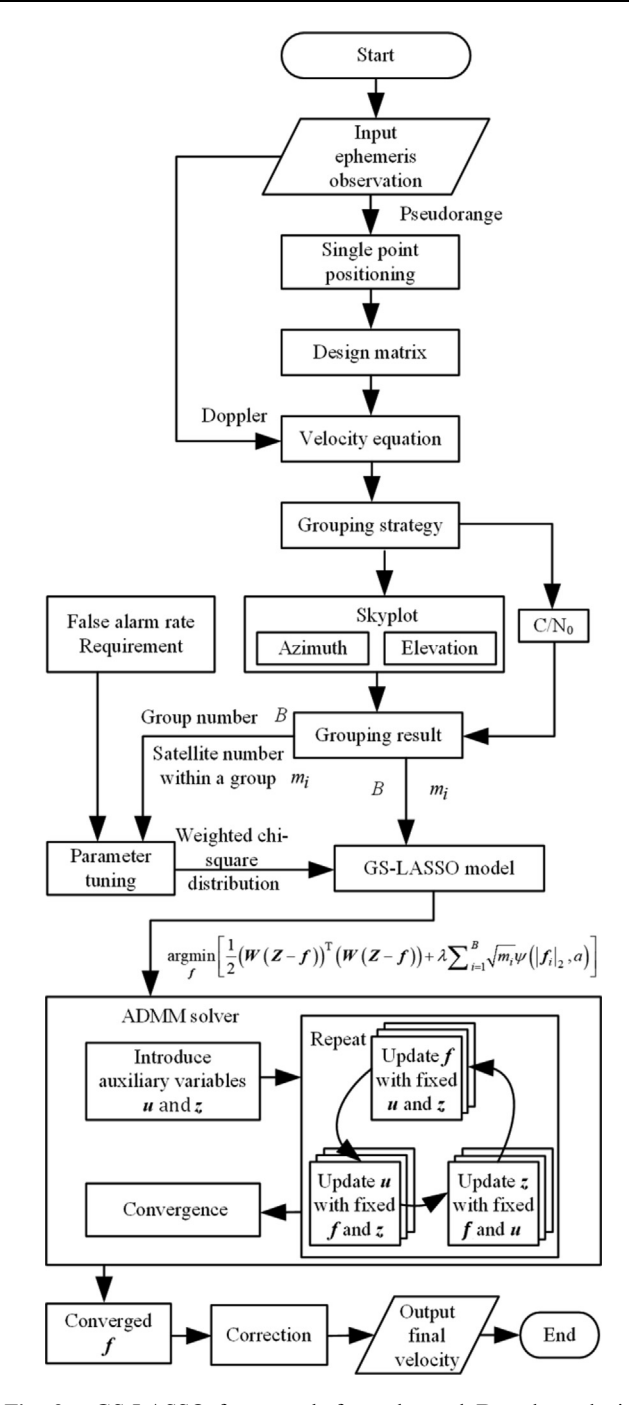


Fig. 2 GS-LASSO framework for enhanced Doppler velocity accuracy.

ing. The flowchart is illustrated in Fig. 2. Our primary contribution is to involve the sparsity-grouping enforcing velocity determination optimization to jointly detect and estimate the impact of multipath/NLOS on Doppler measurements. To facilitate this, the steps are as follows. The first is to use the geometric information of the sky map and  $C/N_0$  for grouping. Second, we can calculate  $\lambda$  based on grouping information and false alarm rate requirements for parameter tuning, since the distribution of the parameter  $\lambda$  can be overbounded by the weighted chi-square distribution. The third is to use the Alternating Direction Method of Multipliers (ADMM) algorithm to cyclically calculate Doppler outliers. Finally, correcting

for the outliers induced by multipath/NLOS as estimated by GS-LASSO can result in a higher estimation accuracy.

### 3.1. Grouping-sparsity-promoting multipath/NLOS mitigation model establishment

Owing to the presence of flat point reflectors, direct signals are affected to introduce the extra reflected signals arriving from similar directions. Consequently, multipath/NLOS is provoked by the associated measurements. In urban areas, the common assumption of multipath/NLOS independence within aviation domain lacks feasibility. Therefore, we adopt an assumption that multipath/NLOS of different satellites are interrelated if they share some identical characteristics.<sup>23</sup> Under this assumption, satellites can be grouped based on prior information. It is assumed that each group of satellites is subject to multipath/NLOS simultaneously, while the presence of multipath/NLOS interference between different groups is considered independent.

The generic group LASSO is introduced to incorporate the group sparsity. Consider f is partitioned into B non-overlapping groups, namely

$$f = \begin{bmatrix} f_1 \\ f_2 \\ \vdots \\ f_R \end{bmatrix} \tag{15}$$

where the dimension of  $f_i$  is  $m_i$ , i = 1, 2, ..., B.  $m_i$  is the *i*th group length. The summary of  $m_i$  equals the dimension of f as n. The split method can be done based on the prior knowledge. Then, the multipath/NLOS mitigation method can be cast as the following unconstrained optimization problem as<sup>35</sup>

$$\underset{f}{\operatorname{argmin}} \left[ \frac{1}{2} (\boldsymbol{W}(\boldsymbol{Z} - \boldsymbol{f}))^{\mathrm{T}} (\boldsymbol{W}(\boldsymbol{Z} - \boldsymbol{f})) + \lambda \sum_{i=1}^{B} \sqrt{m_i} |\boldsymbol{f}_i|_2 \right]$$
(16)

where the generic group Lasso cost, represented as  $\sum_{i=1}^{B} \sqrt{m_i} |f_i|_2$ , serves as an intermediary between the  $l_1$ -norm and  $l_2$ -norm cost. It collectively diminishes group-wise contributions  $\{f_i\}$ , ensuring zero contributions from irrelevant groups. Note that a special case is when  $m_i = 1$  for i = 1, 2, ..., B, namely, each group contains only one element. Eq. (16) returns with the LASSO problem. In instances where observations suffer from contamination, only the grouping substantial outliers are highlighted, while the uncontaminated measurements in other groups are near zero.

Researches show that the cost functions in Eq. (16) tend to underestimate the signal amplitude and sparsity in practice. <sup>34</sup> This will lead to inaccurate estimation and correction of f. As a compensation, non-convex costs have gained popularity. <sup>36–38</sup> It surpasses the  $l_1$ -norm in promoting group sparsity and producing more precise estimations of multipath/NLOS. In this paper, we consider an arctangent cost to replace the generic group LASSO whose cost is  $\sum_{i=1}^{B} \sqrt{m_i} |f_i|_2$ . The optimization problem in the GS-LASSO is

$$\underset{f}{\operatorname{argmin}} \left[ \frac{1}{2} (\boldsymbol{W}(\boldsymbol{Z} - \boldsymbol{f}))^{\mathsf{T}} (\boldsymbol{W}(\boldsymbol{Z} - \boldsymbol{f})) + \lambda \sum_{i=1}^{B} \sqrt{m_{i}} \psi(|\boldsymbol{f}_{i}|_{2}, a) \right]$$
(17)

where a > 0 determines the non-convex degree of the cost. For any constant t, the arctangent cost  $\psi(t,a)$  and its first-order derivative of  $\dot{\psi}(t,a)$  read <sup>34</sup>

$$\psi(t,a) = \frac{2}{a\sqrt{3}} \left( \arctan\left(\frac{1+2a|t|}{\sqrt{3}}\right) - \frac{\pi}{6} \right)$$
 (18)

$$\dot{\psi}(t,a) = \frac{\text{sgn}(t)}{1 + a|t| + a^2 t^2} \tag{19}$$

where sgn(t) is the sign function. Since  $t = |f_i|_2$  here, sgn(t) is always 1. When the scalar parameter a approaches zero, the GS-LASSO approaches the generic group lasso. Fig. 3 depicts the cost functions of the cost and the associated first derivatives. Clearly, the one-dimension function profiles show the arctangent cost has the better ability to approach the  $l_0$ -norm. Compared with the case where a = 0.1, when a is larger (a = 1), the arctangent cost function approximates the  $l_0$ -norm more closely. Therefore, the solution of the non-convexity optimization shares more similarity with the optimization as Eq. (12). Overall, the non-convex cost cannot only enhance the sparsity but also maintain the amplitude of the multipath/NLOS.

However, non-convex costs may make the overall problem stuck in shallow local minima and results in inaccurate solution. To address this problem, we should notice that  $(W(Z-f))^T(W(Z-f))$  is a convex function. Since a parameterizes the non-convexity of the cost, if an appropriate value is chosen, Eq. (17) can still be a convex function. Therefore, the restriction of a can make the final solution converged,  $^{36}$  which needs to be considered in the solver design.

#### 3.2. Multipath/NLOS grouping strategy

A preprocessing strategy for multipath/NLOS grouping is proposed to address the spatial dependence of multipath/NLOS in urban areas. If redundant sensors such as fisheye cameras are available, the integrated information can be utilized to design the grouping strategy. <sup>39,40</sup> However, since these sensors are not always accessible to GNSS users, GS-LASSO focuses primarily on grouping based on GNSS-only features.

Following insights from Ref. 23, elevation angle and azimuth angle are initially chosen as inputs for multipath/NLOS grouping. These features are selected because satellites with similar geometric positions may be obstructed simultaneously by the same buildings. However, GNSS signals from satellites with similar azimuth and elevation angles may still encounter varying multipath/NLOS effects in dynamic environments. The C/N<sub>0</sub> values may significantly differ among satellites with similar elevation and azimuth angle.<sup>24</sup> This arises because C/ N<sub>0</sub> is sensitive to whether GNSS signals are affected by reflection, refraction, diffraction, or non-line-of-sight reception. Consequently, C/N<sub>0</sub> serves as a third parameter for multipath/NLOS grouping. Significantly, C/N<sub>0</sub>, elevation angle and azimuth angle are generally accessible at every receiver.  $C/N_0$  is directly gauged by the receiver, while elevation angle and azimuth angle are calculated by known satellite positions using their present coordinates from the real-time ephemeris. In summary, for GNSS-only users, three GNSS based features are fully utilized. These three features have also been used extensively in the identification of GNSS LOS and NLOS/mul-

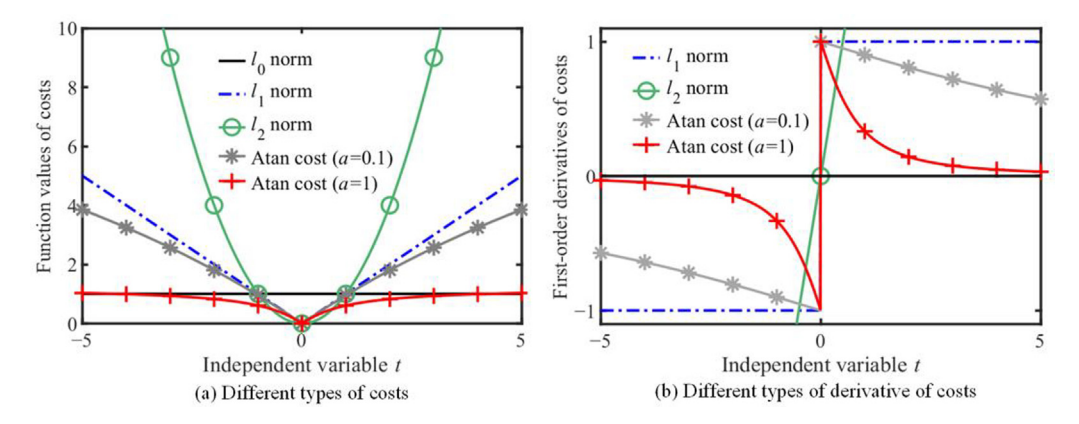


Fig. 3 Sparsity-inducing costs and the first-order derivatives of costs.

tipath in the previous references.<sup>41–43</sup> If all the characteristics of two satellites are similar, they will be likely to be contaminated at the same time.

Therefore, a preliminary sky-plot-based is implemented with the following rule: (A) the satellites should be first separated into segments according to the elevation angle, i.e.  $\theta_{el} > 80^{\circ}, \ 60^{\circ} \leqslant \theta_{el} \leqslant 80^{\circ}, \ 40^{\circ} \leqslant \theta_{el} < 60^{\circ}$  and  $\theta_{el} < 40^{\circ}.$   $\theta_{el}$  is the elevation angle in degrees. (B) For the case where  $60^{\circ} \leqslant \theta_{el} \leqslant 80^{\circ}, \ \text{start}$  counting in ascending order of the PRN number and observe if there are any other satellites are within the 25 ° azimuth range of the current satellite. If so, group these satellites together. If not, repeat this process for the next satellite until all satellites have been grouped. This also applies to the case where  $\theta_{el} < 40^{\circ}$  and  $40^{\circ} \leqslant \theta_{el} < 60^{\circ}.$  (C) For all groups, the group needs to be split again based on the C/N<sub>0</sub>. Satellites with C/N<sub>0</sub> greater than the empirical value are divided into sub-groups. Conversely, the remaining satellites are divided into another group.

To facilitate the rule (C), the relationship between the signal quality curve and elevation angle is fitted. Third-order polynomials are applied to fit data using the least squares criterion, with corresponding uncertainties then calculated. A trial detection threshold, comprising the mean plus standard deviation, is computed. Similar approaches have been reported for such threshold. If measurements fall above this curve, they are considered unaffected by NLOS or multipath effects; otherwise, they are deemed affected by NLOS/multipath. The threshold  $T_{\rm C/N_0}$  as a function of elevation angles is given by

$$T_{C/N_0} = A + B\theta_{el} + C(\theta_{el})^2 + D(\theta_{el})^3$$
 (20)

where A, B, C and D are parameters to be fitted. Fig. 4 presents the  $C/N_0$  test results recorded over a 24 h period under open-sky conditions. The signals utilized include those from GPS L1, BDS B1I, GAL E1, GLONASS L1, and QZSS L1. As B1C signal is currently unavailable in this paper, its potential use will be considered in future studies. Due to the varying  $C/N_0$  distributions among different satellite constellations, Figs. 4(a)–(e) presents the fitting results for each constellation. Additionally, Fig. 4(f) shows the fitting result obtained by combining all constellations. The values are dependent on the specific antenna and receiver being used, meaning they will vary based on the equipment.

The parameters of Eq. (20) for  $C/N_0$  grouping are outlined in Table 1. In our ongoing experiment, the results from Figs. 4(a–e) are employed in our subsequent Experiment 1,

yielding more precise results when the same receiver is used. For the publicly available data in Experiments 2 and 3, the results from Fig. 4(f) are utilized. This is because the  $C/N_0$  pattern is related to the user receiver and antenna. Since the hardware in the public dataset is different, we use data in Fig. 4(f) for Experiments 2 and 3. Fig. 4(f) can illustrate the trend between  $C/N_0$  and elevation angle, and it offers reliable velocity estimation when utilizing different hardware.

After multipath/NLOS grouping, it is assumed that the multipath/NLOS across each group is independent.

#### 3.3. Solver for GS-LASSO

GS-LASSO does not have a closed-form solution, necessitating the design of an appropriate solver. The alternating direction method of multipliers (ADMM) is employed for this purpose. The whole target function expressed in Eq. (17) can be decomposed into some sub-problems. This decomposition facilitates the optimization of one variable while holding the others constant. The detailed derivation is provided below.

According to the ADMM, Eq. (17) is reformatted as a constrained optimization problem

$$\underset{f}{\operatorname{argmin}} \frac{1}{2} \boldsymbol{u}^{\mathsf{T}} \boldsymbol{u} + \lambda \sum_{i=1}^{B} \sqrt{m_{i}} \psi(|\boldsymbol{f}_{i}|_{2}, a)$$
s.t.  $\boldsymbol{u} = \boldsymbol{W} \boldsymbol{Z} - \boldsymbol{W} \boldsymbol{f}$  (21)

Here u is the introduced variable for constructing the ADMM formulation. The augmented Lagrangian function of Eq. (21) is considered as

$$L(\mathbf{f}, \mathbf{z}, \mathbf{u}) = \frac{1}{2} \mathbf{u}^{\mathsf{T}} \mathbf{u} + \lambda \sum_{i=1}^{B} \sqrt{m_i} \psi(|\mathbf{f}_i|_2, a)$$
$$- \mathbf{z}^{\mathsf{T}} (\mathbf{W} \mathbf{f} + \mathbf{u} - \mathbf{W} \mathbf{Z}) + \frac{\eta}{2} |\mathbf{W} \mathbf{f} + \mathbf{u} - \mathbf{W} \mathbf{Z}|_2^2$$
(22)

where z denotes the Lagrangian multiplier vector.  $|Wf + u - WZ|_2^2$  is the squared  $l_2$ -norm of Wf + u - WZ. The parameter  $\eta$  is an auxiliary parameter.

Before the deviation, the meaning of the expression is clarified to avoid ambiguity. First,  $f^k$ ,  $u^k$  and  $z^k$  are the results of the kth iteration in the ADMM. They are constant vectors whose values are fixed. Second, f, u, and z are vector-typed random variables to be optimized in the k+1th iteration. Such variables can be differentiated. Third,  $f^{k+1}$ ,  $u^{k+1}$  and  $z^{k+1}$  are the results of the k+1th iteration. The  $f^{k+1}$ ,  $u^{k+1}$  and  $z^{k+1}$ 

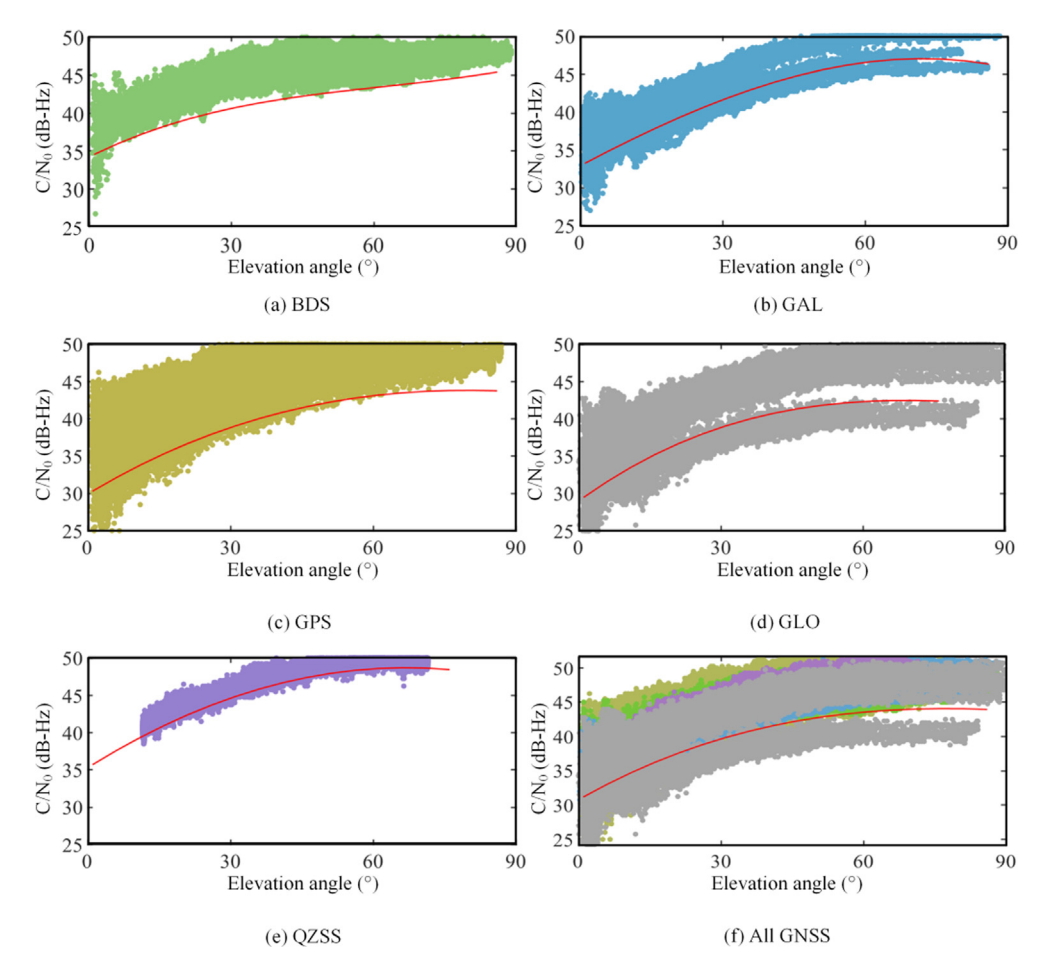


Fig. 4 Elevation angle -  $C/N_0$  curve with  $C/N_0$  threshold  $T_{C/N_0}$  and their source data.

Parameter	Constellation						
	BDS	GAL	GPS	GLO	QZSS	All	
$\overline{A}$	34.57	33.22	30.30	29.46	35.70	31.17	
В	0.31	0.33	0.39	0.46	0.40	0.39	
$C(10^{-3})$	-3.9	-1.1	-3.1	-4.9	-3.0	-3.5	
$D(10^{-5})$	2.10	-1.10	0.58	-1.50	0	0.84	

are also constant vectors. Overall, f, u, and z without the superscript k represent random variables, while those with the superscript k. or k+1 represent constant vectors. Note the random variable f to be optimized in the k+1th iteration is independent from the constant vector  $f^k$ . In other words,  $\partial (f^k)/\partial f = \mathbf{0}$ . In addition, subscripts i represent the ith group. Taking  $f_i$  as an example, this represents extracting the element corresponding to the ith group in the random variable f.

Therefore, we can iterate f, u and z until the ADMM is converged. The fundamental step is as follows. In the k+1th iteration, we first substitute the random variables u and z in Eq. (22) with the constant vectors  $u^k$  and  $z^k$  from the kth iteration. Therefore, the multivariable optimization problem is converted into a single-variable optimization problem regarding the variable f. The optimization solution is  $f^{k+1}$ .

Subsequently, substitute the random variables f and z in Eq. (22) with the known constant vectors  $f^{k+1}$  and  $z^k$ . Therefore, the multivariable optimization problem is converted into a single-variable optimization problem regarding the variable u. The optimization solution is  $u^{k+1}$ . Similarly, we use the known  $f^{k+1}$  and  $u^{k+1}$  to solve for  $z^{k+1}$ . The specific process is as follows.

#### **Step 1.** Update f with $u^k$ and $z^k$

By making the values of u and z fixed, the optimization problem of Eq. (22) can be transformed as

$$f^{k+1} = \arg\min_{f} \lambda \sum_{i=1}^{B} \sqrt{m_i} \psi(|f_i|_2, a)$$
$$- (z^k)^{\mathrm{T}} (Wf + u^k - WZ) + \frac{\eta}{2} |Wf + u^k - WZ|_2^2$$
(23)

Since the matrix W is not an identity matrix,  $f^{k+1}$  cannot be directly decomposed into separated groups. To update f in a simpler and easier manner, inspired by Ref. 45, a slack proximal term to Eq. (23) is added as follows:

$$f^{k+1} = \arg\min_{f} \lambda \sum_{i=1}^{B} \sqrt{m_i} \psi(|f_i|_2, a) - (z^k)^{\mathrm{T}} W f$$
$$+ \frac{\eta}{2} |W f + u^k - W Z|_2^2 + \frac{1}{2} |f - f^k|_S^2$$
(24)

where  $S = \eta(\sigma I - W^T W)$  is a positive semidefinite matrix.  $\sigma$  is a weighted parameter to control the proximity of f to  $f^k$ .  $\sigma$  is required to be not less than the spectral radius of  $W^T W$ . Since W is an idempotent matrix, therefore  $\sigma$  can be chosen slightly above 1 in practice. I is an identity matrix whose dimension equals that of  $W^T W$ .  $|f - f^k|_S^2$  is the semi-norm introduced by the seminner product related with S, given by

$$|f - f^{k}|_{S}^{2} = (f - f^{k})^{\mathrm{T}} \eta (\sigma I - W^{\mathrm{T}} W) (f - f^{k})$$

$$= \eta \sigma |f - f^{k}|_{2}^{2} - \eta (f - f^{k})^{\mathrm{T}} (W^{\mathrm{T}} W) (f - f^{k})$$
(25)

Therefore, we have

$$f^{k+1} = \arg\min_{f} \left\{ \lambda \sum_{i=1}^{B} \sqrt{m_{i}} \psi(|f_{i}|_{2}, a) + \frac{\eta \sigma}{2} f^{\mathsf{T}} f + f^{\mathsf{T}} \left[ -\mathbf{W}^{\mathsf{T}} (\mathbf{z}^{k})^{\mathsf{T}} + \eta \mathbf{W}^{\mathsf{T}} (\mathbf{u}^{k} - \mathbf{W}\mathbf{Z}) - \eta \sigma f^{k} + \eta \mathbf{W}^{\mathsf{T}} \mathbf{W} f^{k} \right] \right\}$$
(26)

The term  $-\boldsymbol{W}^{\mathrm{T}}(\boldsymbol{z}^{k})^{\mathrm{T}} + \eta \boldsymbol{W}^{\mathrm{T}}(\boldsymbol{u}^{k} - \boldsymbol{W}\boldsymbol{Z}) - \eta \sigma \boldsymbol{f}^{k} + \eta \boldsymbol{W}^{\mathrm{T}} \boldsymbol{W} \boldsymbol{f}^{k}$  is irrelevant with  $\boldsymbol{f}$  because the constant vector  $\boldsymbol{f}^{k}$  is independent of the random variable  $\boldsymbol{f}^{.45}$ . An auxiliary term  $\left| -\boldsymbol{W}^{\mathrm{T}}(\boldsymbol{z}^{k})^{\mathrm{T}} + \eta \boldsymbol{W}^{\mathrm{T}}(\boldsymbol{u}^{k} - \boldsymbol{W}\boldsymbol{Z}) - \eta \sigma \boldsymbol{f}^{k} + \eta \boldsymbol{W}^{\mathrm{T}} \boldsymbol{W} \boldsymbol{f}^{k} \right|_{2}^{2} / \eta \sigma$  can be directly added to Eq. (26). A scaled term is reformulated as

$$f^{k+1} = \arg\min_{f} \left\{ \lambda \sum_{i=1}^{B} \sqrt{m_i} \psi(|f_i|_2, a) + \frac{\eta \sigma}{2} |f - \gamma^k|_2^2 \right\}$$
 (27)

where  $\gamma^k = f^k + W^T (\eta WZ - \eta Wf^k - \eta u^k + z^k)/(\eta \sigma) = f^k + W(\eta Z - \eta f^k - \eta u^k + z^k)/(\eta \sigma)$ . Compared with Eq. (23), the matrix before f is an identity matrix instead of W. This drives us to separate variables and obtain updates of each group as

$$f_i^{k+1} = \arg\min_{f_i} \left\{ \psi(|f_i|_2, a) + \frac{1}{2\mu_{(i)}} |f_i - \gamma_i^k|_2^2 \right\}$$
 (28)

where  $\mu_i = \lambda \sqrt{m_i}/(\eta \sigma)$ . There is no closed-form solution for Eq. (28) because of the introduction of the arctangent cost. Fortunately, guided by a recent research, <sup>37</sup> Eq. (28) can be solved by taking its first order derivative with respect to  $f_i$  and setting it to **0**. The formulation is

$$\mu_i \frac{f_i}{|f_i|_2} \dot{\psi}(|f_i|_2, a) + f_i - \gamma_i^k = \mathbf{0}$$
 (29)

A sufficient and necessary condition to make the solution  $f_i$  of Eq. (29) be the solution of Eq. (28) is that Eq. (28) is a convex function. Fortunately, Eq. (28) is strictly convex if and only if

$$\mu_i a < 1 \tag{30}$$

This property has been rigorously proven in Ref. 36 and has been applied in several studies. 34,37,38 With suitable

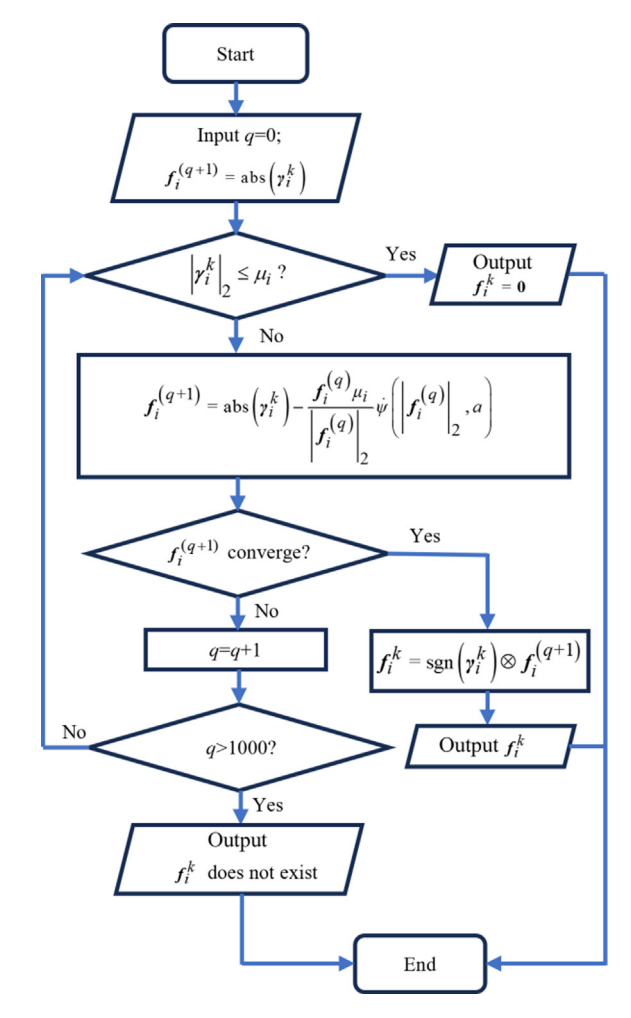


Fig. 5 Flowchart of fixed point iteration scheme to solve Eq. (29).

parameters, the calculated  $f_i$  in Eq. (29) is the global optimal solution. Herein, we can use the fixed-point method to handle the problem in Eq. (29). The flowchart of fixed-point iteration scheme can be seen in Fig. 5. We mark (q) in the superscript of  $f_i$ , representing the qth iteration in the process of solving the fixed-point function.  $\otimes$  represents multiplying by elements between two vectors. Due to the property of the fixed-point iteration,  $f_i^{(q)}$  converges with a linear rate to the unique root  $f_i^k$ . The proof of the convergence of the fixed-point method can be seen in Ref. 37.

After getting the final converged  $f_i^k$ , this process is repeated for elements in each group. Results of each group are stacked together to form the final  $f^k$ .

Step 2. Update u with  $f^{k+1}$  and  $z^k$ 

By making the values of f and z fixed, the optimization problem can be transformed as

$$\boldsymbol{u}^{k+1} = \arg\min_{\boldsymbol{u}} \frac{1}{2} \boldsymbol{u}^{\mathrm{T}} \boldsymbol{u} - (\boldsymbol{z}^{k})^{\mathrm{T}} (\boldsymbol{W} \boldsymbol{f}^{k+1} + \boldsymbol{u} - \boldsymbol{W} \boldsymbol{Z})$$

$$+ \frac{\eta}{2} |\boldsymbol{W} \boldsymbol{f}^{k+1} + \boldsymbol{u} - \boldsymbol{W} \boldsymbol{Z}|_{2}^{2}$$
(31)

By adding  $(z^k)^T z^k / (2\eta)$ , a scaled version can be obtained as

$$\mathbf{u}^{k+1} = \arg\min_{\mathbf{u}} \frac{1}{2} \mathbf{u}^{\mathrm{T}} \mathbf{u} + \frac{\eta}{2} \left| \mathbf{W} \mathbf{f}^{k+1} + \mathbf{u} - \mathbf{W} \mathbf{Z} - \frac{\mathbf{z}^{k}}{\eta} \right|_{2}^{2}$$
(32)

The minimum value is calculated when the derivation of Eq. (32) equals zero. After simple manipulation, the solution is

$$\boldsymbol{u}^{k+1} = \frac{\eta}{1+\eta} \left[ \boldsymbol{W} \boldsymbol{Z} + \frac{\boldsymbol{z}^k}{\eta} - \boldsymbol{W} \boldsymbol{J}^{k+1} \right]$$
 (33)

**Step 3.** Update z with fixed  $u^{k+1}$  and  $f^{k+1}$ 

By fixing  $u^{k+1}$  and  $f^{k+1}$ , a simple criterion to update z is as

$$z^{k+1} = z^k - \eta (W f^{k+1} + u^{k+1} - W Z)$$
(34)

After conducting the three steps for all groups, we must determine whether the used ADMM can present a reliable result. Fortunately, the estimation can be ensured to converge to the underlying ground-truth value, as shown in Appendix B.<sup>46</sup> Therefore, the stopping criterion can be

$$\begin{cases}
 r^{k+1} = \left| \mathbf{u}^{k+1} - \mathbf{W}\mathbf{Z} + \mathbf{W}\mathbf{f}^{k+1} \right|_{2} \leq 10^{-2} \\
 s^{k+1} = \frac{\left| f^{k} - f^{k+1} \right|_{2}}{\max \left\{ \left| f^{k+1} \right|_{2}, 1 \right\}} \leq 10^{-2}
\end{cases}$$
(35)

The first metrics measure the difference between u and WZ - Wf. The second metrics measure the differences between f in adjacent loops. The upper bound of the iteration number is chosen as 1 000. If the ADMM does not converge, no output is presented. Overall, the procedure of the ADMM to solve the GS-LASSO has been derived. To facilitate the actual practice, the algorithm is listed in Algorithm 1. After getting f, Eq. (9) is calculated to output X.

#### Algorithm 1. ADMM solvers for solving GS-LASSO.

**Input**: regularization parameter  $\lambda$ , auxiliary parameter  $\eta$ , nonconvexity parameter a, weighted parameter  $\sigma$ 

#### Output: $f^{k+1}$

- 1. Initialize:  $f^0 u^0, z^0$
- 2. for  $k = 0, 1, 2 \cdots, 1000$  until convergence do
- 3.  $\gamma^k = f^k + W(\eta Z \eta f^k \eta u^k + z^k)/(\eta \sigma)$
- 4. for  $i = 1, 2, \dots, B$  do
- 5.  $\mu_i = \lambda \sqrt{m_i}/(\eta \sigma)$
- 6. if a > 0//GS-LASSO
- 7.  $f_i^{k+1}$  solved according to Fig. 5
- 8. end if

- 10.  $f^{k+1} \leftarrow \text{stack } f_i^{k+1}, i = 1, 2, \dots, B / / \text{Step 1}$ 11.  $u^{k+1} = \eta (WZ + z^k / \eta Wf^{k+1}) / (1 + \eta) / / \text{Step 2}$ 12.  $z^{k+1} = z^k \eta (Wf^{k+1} + u^{k+1} WZ) / / \text{Step 3}$

#### 3.4. Time complexity analysis

The time complexity of ADMM solvers is now examined. The time complexity is dominated by three steps in each iteration. For the Step 1, the time complexity to compute  $\gamma^k$  is  $O(n^2)$  and the time complexity to solve Eq. (29) is  $O(N_{\text{fixed}}n)$ , where  $N_{\text{fixed}}$ is the iteration number for the fixed-point method to converge.  $N_{\text{fixed}}$  can be approximately estimated as  $N_{\text{fixed}} = \log_{L_1}(\varepsilon_1)$ , where  $0 < L_1 < 1$  is the Lipschitz constant and  $\varepsilon_1$  is the

expected accuracy of the convergence error.<sup>47</sup> In practice,  $N_{\text{fixed}}$  is typically less than 30. For the Steps 2 and 3, the computational cost is around  $O(n^2)$ . The time complexity cost in an iteration for ADMM is  $O(n^2 + N_{\text{fixed}}n)$ . Therefore, the final ADMM using has a complexity  $O(N_{\text{ADMM}}n^2 + N_{\text{ADMM}}N_{\text{fixed}}n)$ .  $N_{\text{ADMM}}$  represents the number of iterations required for ADMM to converge, typically scales as  $O(1/\varepsilon_2)$  based on ADMM convergence theory.<sup>48</sup>  $\varepsilon_2$  is the expected accuracy error of the ADMM. For moderate values of  $N_{\text{fixed}}$ , the magnitude of  $N_{\text{ADMM}}$  significantly impacts the computational efficiency of GS-LASSO. In practice, addressing ADMM problems does not demand heavy resources. GS-LASSO simply includes executing a sequence of mathematically tractable updates, rendering it computationally feasible.

By comparison, the complexity of the standard LS is  $O(n^3)$ , which is generally smaller than  $O(N_{\text{ADMM}}n^2 + N_{\text{ADMM}}N_{\text{fixed}}n)$ . The complexity of the MHSS can be noted as 49

$$O\left(n^{3}\left(1+\sum_{a=1}^{\varpi}\frac{n!}{a!(n-a)!}\right)+(n-1)^{3}\left(1+\sum_{a=1}^{\varpi-1}\frac{(n-1)!}{a!(n-a-1)!}\right)\right)$$
(36)

where  $\varpi$  is the number of the satellites polluted by the multipath/NLOS. The greatest computational load comes from the combinatorial numbers. In a typical urban environment with multi-constellations, as  $\varpi$  and n increase, the load introduced by the combinatorial numbers will exceed that introduced by  $N_{\rm ADMM}$ . The computational burden for MHSS is much higher than the GS-LASSO.

#### 4. Performance analysis of GS-LASSO

As mentioned earlier, inspired by FDE, GS-LASSO can perform detection and correction operation. Therefore, similar to FDE, false alarm rate and detection ability must be considered in the detection process. This section examines the relationship between the regularization parameter and the false alarm rate, providing a parameter-tuning criterion. Due to the complexity of GS-LASSO, directly analyzing the missed detection rate is challenging. Thus, this section establishes sufficient conditions of the minimum detectable multipath/NLOS. Finally, situations where GS-LASSO performance may degrade are discussed.

#### 4.1. Parameter tuning of Lagrange multiplier $\lambda$ accommodating false alarm rate

In the GS-LASSO, the Lagrange multiplier  $\lambda$  works as a tuning parameter. The value of  $\lambda$  exerts heavy influence on the estimated solution. An over-large  $\lambda$  will make all regression coefficients tend to be zero. Conversely, an excessively small  $\lambda$  will make Z approaches f. Hence, many fault-free candidates will be regarded as the faulty, making the FDC not reliable, which is the case of false alarm. In the LASSO-related problems, there are mainly two methods to conduct parameter tuning. First, the information criterion is intensely used to select real-time  $\lambda$ , such as the generalized cross-validation and Akaike information criterion. 13 Second, a fixed  $\lambda$  can be calculated from the training data collected before.<sup>20</sup> However, as discussions in Ref. 50, LASSO can also be seen as a progress containing detection.

From this perspective, in the multipath/NLOS-free case, the estimated *f* should be a zero vector. If this is not satisfied, a false alarm event exists. Unfortunately, the currently tuning methods fail to consider this. Namely, the Required Navigation Performance (RNP) is not fully considered.

Hence, for RNP, the relationship between  $\lambda$  and the false alarm rate is taken into account.  $\lambda$  is tuned to ensure the false alarm probability will not exceed the required value. This will be beneficial to grant the user with sufficient continuity performance in the navigation task.

In a multipath/NLOS-free case, to ensure no false alarm is presented, the estimated f needs to be a zero-vector. There is a finite sequence of transition points  $\lambda_1^* > \lambda_2^* > ... > \lambda_n^* = 0.^{51}$  When  $\lambda$  exists between two adjacent transition points, the number of non-zero elements in f keeps unchanged. A special case occurs when  $\lambda$  exceeds the largest transition point  $\lambda_1^*$ , the estimation of f only contains zero. Namely, to avoid false alarm, i.e., to ensure f is a zero-vector, a necessary and sufficient condition is to make  $\lambda \geq \lambda_1^*$ . Therefore, we can build the relationship between  $\lambda$ ,  $\lambda_1^*$  and f for GS-LASSO.

Our first aim is to find the critical  $\lambda_1^*$  to ensure f is the zero vector. The overall objective function of Eq. (17) is non-smooth due to the non-smooth cost. However, the overall objective is convex if Eq. (30) is satisfied. Therefore, instead of the differentiation methods, the sub-gradient method can be employed. For simplicity, we can write the convex objective as

$$F(\mathbf{f}) = \frac{1}{2} (\mathbf{W}(\mathbf{Z} - \mathbf{f}))^{\mathrm{T}} (\mathbf{W}(\mathbf{Z} - \mathbf{f})) + \lambda \sum_{i=1}^{B} \sqrt{m_i} \psi(|\mathbf{f}_i|_2, a)$$
(37)

According to the property of the sub-gradient, a point  $\hat{f} \in \mathbf{R}^n$  minimizes F i.e.,  $\hat{f}$  is the solution to Eq. (17) if and only if  $0 \in \partial F(f)$  at  $\hat{f}$ . For group i  $(1 \le i \le B)$ , the gradient of F(f) evaluated at  $\hat{f}$  reads

$$F(\hat{\mathbf{f}}) = \left[ \mathbf{W}^{\mathrm{T}} (\hat{\mathbf{f}} - \mathbf{Z}) \right]_{i} + \lambda_{i} \sqrt{m_{i}} \mathbf{\kappa}_{i}$$
(38)

where  $\kappa_i$  denotes the sub-gradient of  $\psi(|f_i|_2, a)$  as follows

$$\mathbf{\kappa}_{i} = \begin{cases} \frac{\hat{f}_{i}}{\left(1 + a\left|\hat{f}_{i}\right|_{2} + a^{2}\left|\hat{f}_{i}\right|_{2}^{2}\right)\left|\hat{f}_{i}\right|_{2}} & \hat{f}_{i} \neq \mathbf{0} \\ \in \left\{\mathbf{\kappa}_{i} : \left|\mathbf{\kappa}_{i}\right|_{2} \leqslant 1\right\} & \hat{f}_{i} = \mathbf{0} \end{cases}$$

$$(39)$$

Consequently, for each group,  $\hat{f}_i$  only contains zero elements if the following three conditions hold

$$\nabla F(\mathbf{f}) = (-\mathbf{W}^{\mathsf{T}}\mathbf{Z})_{i} + \lambda_{i}\sqrt{m_{i}}\mathbf{\kappa}_{i}$$

$$\tag{40}$$

$$\hat{\mathbf{f}}_{i} = \left(1 + a|\hat{\mathbf{f}}_{i}|_{2} + a^{2}|\hat{\mathbf{f}}_{i}|_{2}^{2}\right)|\hat{\mathbf{f}}_{i}|_{2}\mathbf{\kappa}_{i}$$
(41)

$$|\mathbf{\kappa}_i|_2 \leqslant 1 \tag{42}$$

Notice that Eq. (41) always holds if  $\hat{f}_i = 0$ , we only need to search  $\lambda$  and  $u_i$  to satisfy Eq. (40) and Eq. (42). The unique solutions are represented as follows,

$$\lambda_i \geqslant \lambda_{1,i}^* = \left| \left( \boldsymbol{W}^{\mathrm{T}} \boldsymbol{Z} \right)_i / \sqrt{m_i} \right|, \tag{43}$$

$$\mathbf{\kappa}_{i} = (\mathbf{W}^{\mathrm{T}}\mathbf{Z})_{:}/(\lambda_{i}\sqrt{m_{i}}) \tag{44}$$

Therefore, the equations represent the necessary and sufficient conditions on  $\lambda$  to make  $\hat{f}_i$  a zero vector. For all groups,

the required  $\lambda^*$  should be the maximum value of all possible  $\lambda_1^*$ . For further simplification,  $\boldsymbol{\Theta}$  is set as a  $B \times 1$  vector whose element contains  $\left| \lambda_{1,i}^* \right|_2$  for i = 1, 2, ..., B. The final  $\lambda_1^*$  is

$$\lambda_1^* = \max \left| \left( \boldsymbol{W}^{\mathrm{T}} \boldsymbol{Z} \right)_i / \sqrt{m_i} \right|_2 = \left| \boldsymbol{\Theta} \right|_{\infty} \tag{45}$$

where max means the maximum element of a vector and  $|\Theta|_{\infty}$  is the infinite norm.

In summary, if  $\lambda$  is tuned according to Eq. (45),  $\hat{f}$  will always be zero. Notice in practice, the specific value of  $|\Theta|_{\infty}$  changes with the observation. But the probability distribution of  $|\Theta|_{\infty}$  should be identical when there is no multipath/NLOS. Therefore, attention is towards the probability distribution function (PDF) of  $|\Theta|_{\infty}$ . We can set the value of  $\lambda$  according to the quantile to the false alarm rate if the distribution of  $|\Theta|_{\infty}$  is available.

Therefore, the second aim is to find  $\lambda$  to make  $P(\lambda > |\Theta|_{\infty}|f=0)$  at a value less than the required false alarm rate. Before the ongoing derivation, finding the accurate distribution of  $|\Theta|_{\infty}$  is hard. A method using Monte Carlo and extreme value theory can be used to estimate the distribution of  $\Theta$  in LASSO, but no method is extended for the GS-LASSO. An alternative method is to consider the probability distribution function of  $I_2$  norm of  $\Theta$  on tuning  $\lambda$ . According to the norm inequality, the following holds

$$|\mathbf{\Theta}|_{\infty} \leqslant |\mathbf{\Theta}|_{2} \tag{46}$$

If  $\lambda < |\mathbf{\Theta}|_{\infty}$ ,  $\lambda$  must be lower than  $|\mathbf{\Theta}|_2$ . Consequently,  $P(\lambda < |\mathbf{\Theta}|_{\infty}) \leq P(\lambda < |\mathbf{\Theta}|_2)$ . This means we only need to assess the value of  $P(\lambda < |\mathbf{\Theta}|_2) = P(\lambda^2 < |\mathbf{\Theta}|_2^2)$ . We further notice

$$|\mathbf{\Theta}|_{2}^{2} = \sum_{i=1}^{B} \left| \left( \mathbf{W}^{\mathrm{T}} \mathbf{Z} \right)_{i} / \sqrt{m_{i}} \right|_{2}^{2}$$

$$= \sum_{i=1}^{B} \left[ \left( \mathbf{I} - \mathbf{H} (\mathbf{H}^{\mathrm{T}} \mathbf{H})^{-1} \mathbf{H}^{\mathrm{T}} \right) \mathbf{Z} \right]_{i} / m_{i}$$
(47)

If  $m_i = 1$ ,  $|\Theta|_2^2$  follow a chi-square distribution with degree of freedom (DOF) as  $n - 3 - n_{\rm cons}$ , where  $n_{\rm cons}$  is the used constellation. However, if  $m_i$  varies, the consideration of the real DOF is not feasible. Consequently, we subsequently ignore their effect, insisting that each element obtained from  $\left(I - H(H^{\rm T}H)^{-1}H^{\rm T}\right)Z$  in the multipath/NLOS-free case is entirely independent. Fortunately, with this inflated DOF, the quantile corresponding to the same false alarm rate also increases and the computed  $\lambda$  is larger. Namely, this guarantees that the false alarm rate remains conservatively lower than the expected performance requirement.

Now we can show the closed-form distribution of  $|\mathbf{\Theta}|_2^2$ . Under the above assumption, the value of  $|\mathbf{\Theta}|_2^2$  can be seen as a summary of chi-square distribution with different weights. Therefore,  $|\mathbf{\Theta}|_2^2$  follows the weighted chi-square distribution. The weights are related with the number of satellites in a group. Its cumulative distribution function (CDF) is given in the Appendix C. <sup>54</sup> Therefore, the value of  $\lambda$  can be obtained as at the false alarm rate  $P_{\rm fa}$  of the weighted chi-square distribution, which is shown as

$$\lambda = h^{-1}(P_{fa}, \boldsymbol{\alpha}, \mathbf{DOF}) \tag{48}$$

where  $h^{-1}$  is the inverse CDF of the weighted chi-square distribution.  $\xi$  is a vector containing weights for each group and **DOF** is a vector signifying the DOF for each group. Some methods to quickly estimate the quantile can be referenced at Ref. 54. Finally, we can ensure  $P(\lambda < |\Theta|_2 | f = 0.) = P(\lambda^2 < |\Theta|_2^2 | f = 0) < P(\lambda < |\Theta|_\infty | f = 0) = P_{\rm fa}$ , which completes our derivation.

Finally, when no multipath/NLOS is detected, Eq. (17) returns with the LS. This means the estimated result of the group LASSO is identical to the least square in the multipath/NLOS-free case. If the multipath/NLOS is detected and corrected, then the improved estimation can be obtained after removing the estimated outliers vector.

#### 4.2. Sufficient detectability analysis

Given that GS-LASSO is applicable in FDC, the ability to detect the magnitude of multipath/NLOS becomes a crucial metric. This mirrors the concept of defining the minimum detectable fault in chi-square RAIM FDE. However, due to the complexity of GS-LASSO, determining the exact value of the minimum detectable error is challenging. Therefore, this paper presents a sufficient condition for GS-LASSO to detect faults. It is important to note that in the presence of additive multipath/NLOS, a detection event can be modeled as  $\{|\Theta|_{\infty} > \lambda|f\neq 0\}$ . Using the norm inequality as

$$\sqrt{n}|\mathbf{\Theta}|_{\infty} > |\mathbf{\Theta}|_{2} \tag{49}$$

where n is the dimension of  $\boldsymbol{\Theta}$ . A sufficient condition to make  $|\boldsymbol{\Theta}|_{\infty} > \lambda$  hold is to make  $|\boldsymbol{\Theta}|_2 > \sqrt{n}\lambda$ . Note that when additive multipath/NLOS exists,  $\boldsymbol{\Theta} = \left[ \left| \left( \boldsymbol{W}^T(\boldsymbol{Z}^* + \boldsymbol{f}) \right)_1 / \sqrt{m_1} \right|_2, \right. \left. \left| \left( \boldsymbol{W}^T(\boldsymbol{Z}^* + \boldsymbol{f}) \right)_2 / \sqrt{m_2} \right|_2, \cdots, \left| \left( \boldsymbol{W}^T(\boldsymbol{Z}^* + \boldsymbol{f}) \right)_B / \sqrt{m_B} \right|_2 \right]$  with  $\boldsymbol{Z}^*$  is the noise free from multipath/NLOS. Therefore,  $|\boldsymbol{\Theta}|_2$  can be shown as

$$|\mathbf{\Theta}|_{2} = \sqrt{\sum_{i=1}^{B} (\mathbf{W}^{\mathrm{T}} \mathbf{Z}^{*})_{i} / \sqrt{m_{i}} + \sum_{i=1}^{B} (\mathbf{W}^{\mathrm{T}} \mathbf{f})_{i} / \sqrt{m_{i}}}$$
 (50)

With the triangle inequality, we have

$$|\boldsymbol{\Theta}|_{2} > \sqrt{\sum_{i=1}^{B} (\boldsymbol{W}^{\mathrm{T}} \boldsymbol{f})_{i} / \sqrt{m_{i}}} - \sqrt{\sum_{i=1}^{B} (\boldsymbol{W}^{\mathrm{T}} \boldsymbol{Z}^{*})_{i} / \sqrt{m_{i}}}$$
 (51)

Therefore, if  $|\Theta|_2 > \sqrt{n}\lambda$  holds, a sufficient condition is

$$\sqrt{\sum_{i=1}^{B} \left(\boldsymbol{W}^{\mathrm{T}} \boldsymbol{f}\right)_{i} / \sqrt{m_{i}}} - \sqrt{\sum_{i=1}^{B} \left(\boldsymbol{W}^{\mathrm{T}} \boldsymbol{Z}^{*}\right)_{i} / \sqrt{m_{i}}} > \sqrt{n}\lambda$$
 (52)

Since  $\sqrt{\sum_{i=1}^{B} (\boldsymbol{W}^{T} \boldsymbol{Z}^{*})_{i} / \sqrt{m_{i}}} < \lambda$  holds in the multipath/NLOS-free case with confidence level at  $1 - P_{\mathrm{fa}}$ , the final sufficient condition is

$$\sum_{i=1}^{B} \left( \mathbf{W}^{\mathrm{T}} \mathbf{f} \right)_{i} / \sqrt{m_{i}} > \left( \sqrt{n} + 1 \right)^{2} \lambda^{2}$$

$$\tag{53}$$

In other words, if multipath/NLOS satisfies Eq. (53), it will be sensed by the proposed GS-LASSO over the confidence level at  $1-P_{\rm fa}$ .

#### 4.3. Limitation

GS-LASSO lies on the assumptions of sparsity and grouping. Consequently, the interruption of these two properties results in performance degradation. For instance, when majority satellites measurements are affected by multipath/NLOS, the sparsity is not met. This compromises the reliability of the results. Moreover, due to the oversight of the influence of difference between the real DOF and the inflated DOF in parameter tuning, when only a few satellites are visible, the relative difference between n and  $n-3-n_{\rm cons}$  is large. Therefore, the parameter  $\lambda$  is too conservative to translate into the good estimation performance. In such circumstances, MHSS emerges as a preferable alternative. For urban users, occlusion from other vehicles, trees, and small obstructions can disrupt the grouping characteristics. In the future, we will consider incorporating sparsity within groups to address this issue.

#### 5. Experimental validation

#### 5.1. Experiment in the typical urban environment

A vehicle field test was conducted to evaluate the performance of the proposed GS-LASSO for Doppler velocity determination in Lujiazui CBD, Shanghai, China. The test took place on September 3, 2022, covering a drive path of approximately 2 700 m. The vehicle mainly navigated in the typical urban area and crossed through some dense urban areas. Some dense urban areas are represented by street viewpoints A, B, and C in Fig. 6(a). During the experiment, GNSS raw measurement data were collected at a sampling rate of 1 Hz using a Terus BX40C receiver. Single-frequency Doppler measurements from multiple constellations, including GPS, Galileo, BDS, and QZSS were utilized for velocity determination. The experimental equipment layout with the used GNSS receiver is displayed in Fig. 6(b). The ground truth is provided by the highsampling-rate GNSS/INS integrated navigation system. The raw measurements from the integrated navigation system are post-processed by the Kalman filter to compute the groundtruth value. Forward and backward processing are performed to maximize trajectory accuracy. The employed INS is as shown in Fig. 6(c). The GINAV software is used to process all data in this section.<sup>55</sup>

To validate the performance of the proposed method, GS-LASSO is compared with other velocity optimization methods. While several existing algorithms  $^{10-15}$  have been developed, these primarily focus on accuracy and do not adequately address other RNP indices, particularly the false alarm rate. Consequently, these algorithms are not directly comparable to GS-LASSO. The algorithms considered for comparison include the standard least squares method and MHSS  $^{19}$ . The false alarm rate for the evaluations is set at 0.05. As an indicator of comparative performance, the velocity errors ( $\nu_E$ ) are calculated. The velocity errors are differences between the real-time output velocity and the post-processing true value.

In this section, to ensure practical execution of the MHSS, two strategies are employed. First, chi-square metrics are used to determine the exclusion order. Second, the number of fault modes is constrained by setting an upper limit on the number of simultaneously faulty satellites. This is to avoid unaccept-

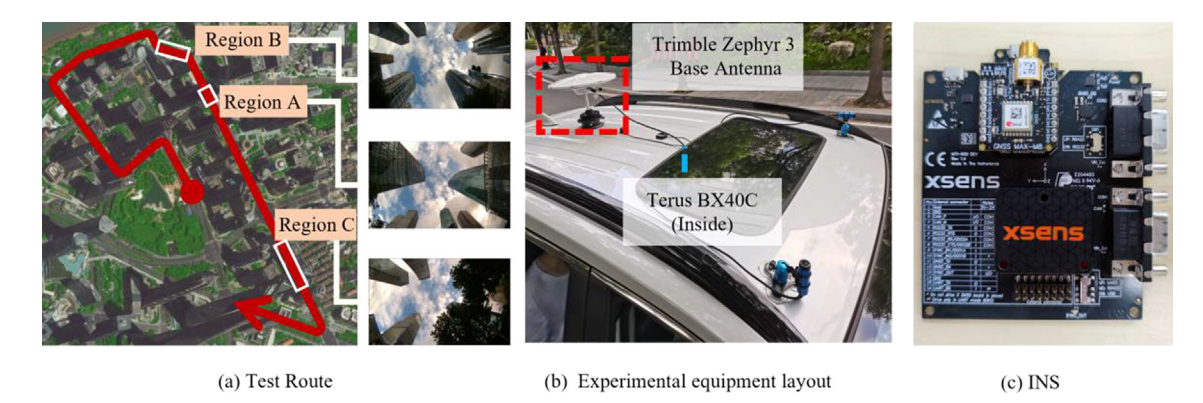


Fig. 6 Test scenario of vehicle test.

able computational loads due to excessively large subsets. If accurate exclusion is not feasible, the subset minimizing the chi-square test statistic is used for velocity estimation. Other parameters are consistent with those in Ref. 19. In addition, GS-LASSO works as the FDC, while the MHSS works as the FDE.

The impact of the sparse assumption on the proposed algorithm is investigated. We use whether MHSS can exclude the satellites as the criterion to rank whether multipath/NLOS exists. This drives us to evaluate the performance of MHSS in successfully excluding satellites affected by multipath/NLOS under different maximum fault numbers. The results are depicted in Fig. 7. Detection alarms are indicated by the green background. It is evident that in urban environments, MHSS issues alert messages at nearly all times. Marked points indicate the successful identification of multipath/NLOS. Unmarked points indicate the MHSS is powerless against issuing a definite exclusion. The results demonstrate that as the number of assumed fault modes  $n_{\text{fault}}$  increase, the proportion of successful exclusions by MHSS also increases. Specifically, for  $n_{\text{fault}}$  equal to 2, 3, and 4, the success rates are 6.9%, 24.0%, and 45.0%, respectively.

We utilize the case where  $n_{\text{fault}}$  is set as 4 to investigate the resultant estimations. If MHSS is capable of eliminating multipath/NLOS, only four or fewer satellites are concurrently affected by multipath/NLOS. Otherwise, more than four satellite measurements are contaminated by multipath/NLOS. We compare the impact of sparsity on GS-LASSO under circumstances where the polluted measurements are either less than or greater than four. A comparison of three-dimensional (3D) velocity errors is presented in Fig. 8. When more than four measurements are corrupted, the estimation deteriorates, as indicated by a higher number of outliers in  $\nu_{\rm E}$  PDF distributions with wider cores and heavier tails. This suggests that the violation of sparse assumption due to the quantity of multipath/NLOS has a noticeable effect on algorithm performance.

Subsequently, the combined impact of grouping-sparsity and arctangent cost function is evaluated. We compare GS-LASSO to the LASSO. LASSO here incorporates neither a new convex cost function nor grouping information. Fig. 9 displays the empirical distribution functions of the  $\nu_{\rm E}$  error for both methods. For the majority of epochs, the distribution of GS-LASSO lies above that of LASSO, suggesting that GS-

LASSO achieves smaller  $v_{\rm E}$ . Statistical analysis further supports this, with LASSO yielding a root mean square error (RMSE) of 0.453 m/s while GS-LASSO attains a smaller value at 0.408 m/s. These results underscore the effectiveness of incorporating group constraints and arctangent cost as prior conditions.

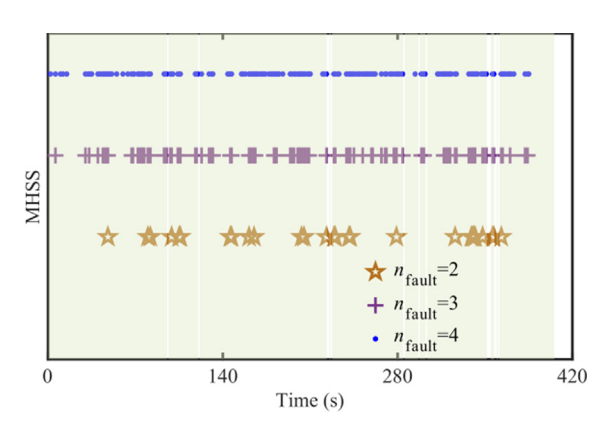


Fig. 7 Sign of exclusion ability of MHSS.

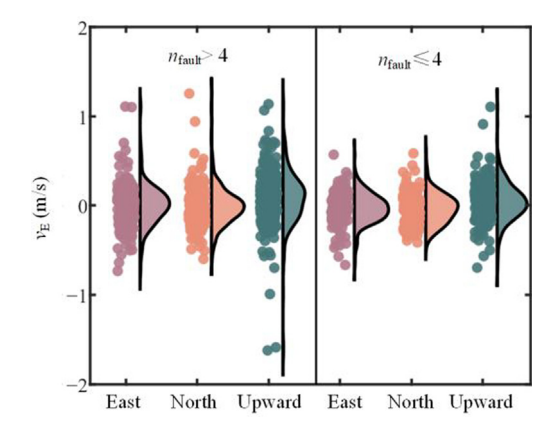
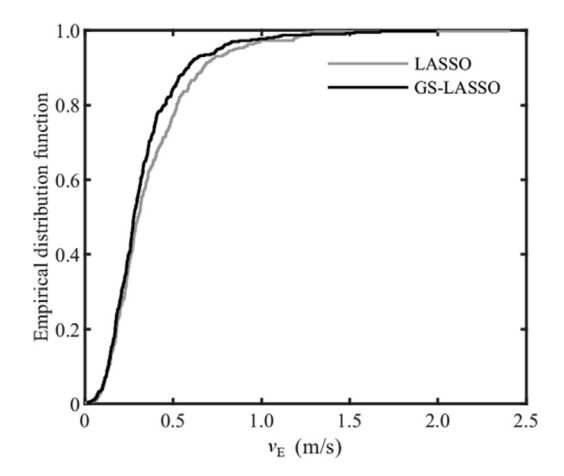


Fig. 8  $v_{\rm E}$  distribution comparison in terms of polluted satellites numbers of GS-LASSO.



**Fig. 9** Distributions of  $v_{\rm E}$  regarding LASSO and GS-LASSO.

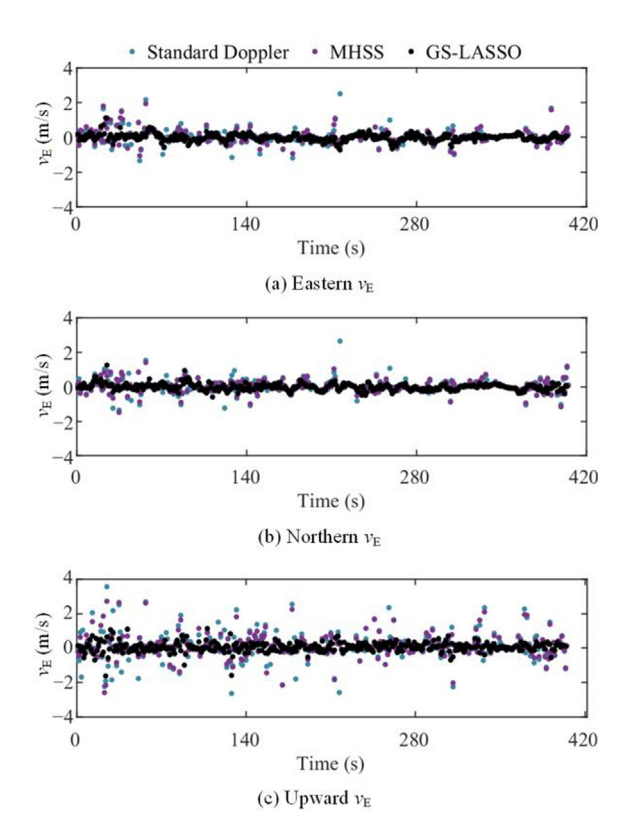


Fig. 10 Doppler measurements-based velocity accuracy with standard LS, MHSS and GS-LASSO.

The velocity estimation performance of the standard LS, MHSS and GS-LASSO is evaluated and scrutinized in terms of  $v_E$ . In this sub-section,  $n_{fault}$  is set three for the MHSS to ensure the MHSS can be conducted in real-time. Fig. 10 presents the time series of  $v_E$  after the optimization according to the eastern, northern, and upward directions. The maximum speed error is in the upward directions with obvious fluctuation. After the optimization, the velocity errors of all three methods demonstrates the enhancement. For MHSS, anoma-

lous velocity errors are detected and excluded through MHSS hypothesis testing. For the GS-LASSO, after the detection and correction, there is also a significant improvement in velocity accuracy.

Since in the urban area, the eastern and the northern errors are always focused on, the horizontal  $v_E$  is analyzed. The twodimensional distributions of horizontal  $v_{\rm E}$  are plotted and fitted with an elliptical curve corresponding to the 95% confidence level in Fig. 11. The errors of GS-LASSO demonstrate a great concentration, characterized by the shortest axis of the ellipse. This suggests that GS-LASSO holds a significant advantage in the horizontal dimension critical for vehicle navigation. The box plot on the top and right side further reinforces this conclusion, with fewer outliers. The incompetence of MHSS to meet performance expectations is due to its inability to accurately exclude multipath/NLOS, particularly evident at a ratio of 24.0% when  $n_{\text{fault}} = 3$ . Although enhancing  $n_{\text{fault}}$ can enhance performance optimization, as discussed later, the computational demands are excessively high, rendering it impossible to achieve real-time performance.

To visualize the advantages of the methods, the 3D velocity error probability distribution in Fig. 12. The  $\nu_{\rm E}$  of the GS-LASSO method has the steepest core and the thinnest tail, highlighting the superiority of the proposed approach. Fig. 13 further summarizes the absolute  $\nu_{\rm E}$  statistics of the three velocity estimation methods, including RMSE, standard deviation (STD), and absolute bias (MEAN). Across all metrics, MHSS demonstrates improvements of 17.1%, 15.5%, and 18.7% in 3D velocity accuracy compared to the original method, as measured by RMSE, STD, and absolute bias, respectively. GS-LASSO method demonstrates significant improvement, with enhancements of 54.6%, 62.5%, and 48.0% over the original velocity estimation method in terms of RMSE, STD, and absolute bias, respectively.

Finally, Fig. 14 summarizes the percentages of various ranges of  $v_E$ . The rings, progressing from the inside out, symbolize GS-LASSO, MHSS and standard Doppler method. Distinct colors signify the percentages of errors associated with each method, falling within various ranges. As expected, due to severe multipath/NLOS effects, the original method exhibits the largest  $v_E$  percentages, reaching 16.9% for  $v_E$  exceeding 1 m/s. With the use of the GS-LASSO method, the percentages are significantly reduced to only 2.0%, demonstrating the smallest  $v_{\rm E}$  among the three methods. This indicates that after optimization, velocity accuracy has almost improved from meters per second to decimeters per second. For velocities ranging from 100 cm/s to 50 cm/s, MHSS and the GS-LASSO methods demonstrate  $v_E$  percentages of over 19.9% and 13.6%, respectively. Conversely, for  $v_E$  less than 50 cm/s, the percentages are notably higher, with values at 67.2% and 84.4% for MHSS and the GS-LASSO, respectively. Overall, GS-LASSO outperforms MHSS in mitigating the multipath/NLOS, because the MHSS method is hard to ensure complete identification of multiple observations under multipath/NLOS contamination in urban areas all the time.

Comparing GS-LASSO with MHSS, their respective average computing times are calculated per epoch in this subsection. For MHSS, the hypotheses respectively involve a maximum of 2, 3, or 4 fault modes. Normalizing these times against the standard least square method, as shown in Table 2, reveals that GS-LASSO time remains consistent regardless of

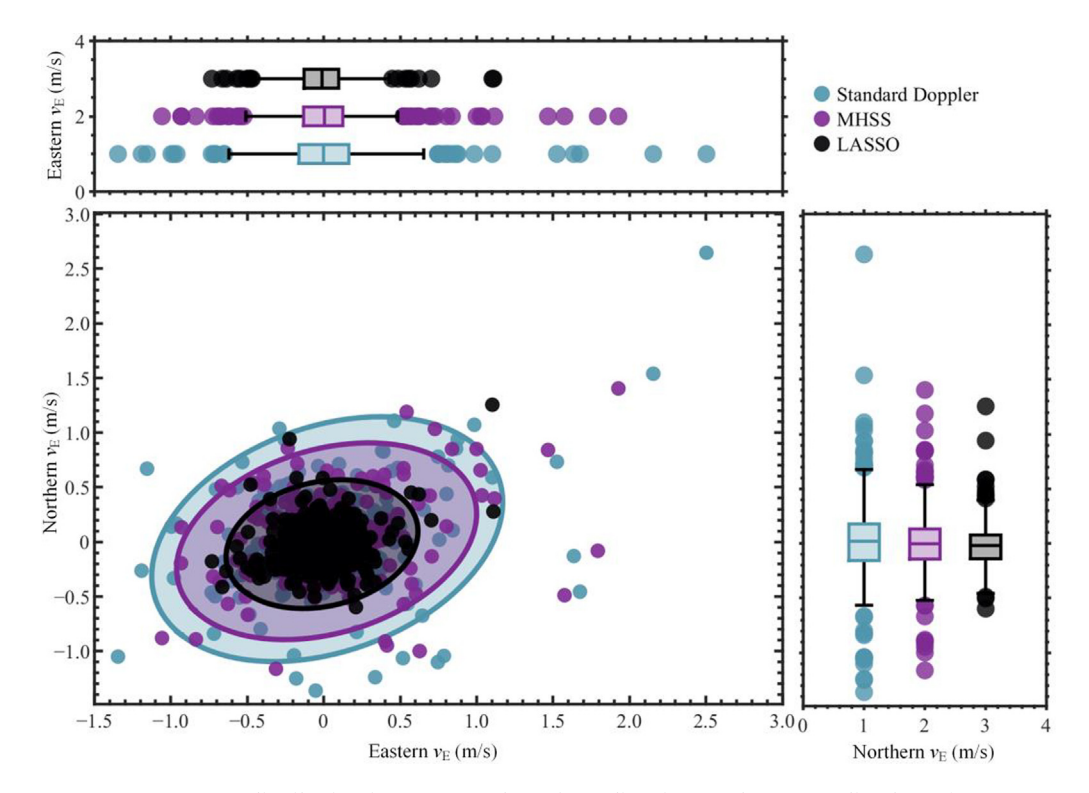


Fig. 11  $v_E$  distribution in eastern and northern directions and corresponding box plot.

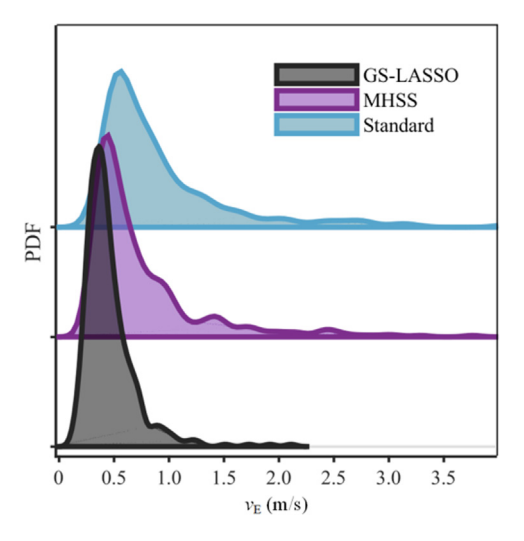


Fig. 12 Approximate probability distribution of 3D  $v_{\rm E}$ .

the number of affected satellites. Its longer processing time due to its non-closed form equation is still less than that of the MHSS, despite using chi-square metrics to optimize the exclusion order. However, MHSS may become ineffective if the number of heavily impacted satellites exceeds 4 in urban areas, leading to a significant increase in processing time. The GS-LASSO processing time is similar to time of MHSS ( $n_{\text{fault}} = 2$ ) and only about one seventh of MHSS ( $n_{\text{fault}} = 3$ ). If  $n_{\text{fault}}$  is 4 or more, the MHSS method becomes intractable in an urban area.<sup>53</sup> This reinforces our earlier finding that

GS-LASSO has a lower computational burden than MHSS, as discussed in Section 3.4.

#### 5.2. Experiment in deep urban environment

We evaluate our proposed algorithm in the deep urban environment in this subsection. The public data, UrbanNav, is chosen to study the GNSS velocity determination in urban canyons. 56 The test takes place on May 21, 2021 with a travel distance at 4.5 km lasting for over 1 500 s in Hong Kong, China. During the experiment, GNSS raw measurement data are collected at a sampling rate of 1 Hz using a ublox-f90P receiver. Single-frequency Doppler measurements from five constellations, including GPS, Galileo, BDS, GLONASS and QZSS are utilized for velocity determination. During the process, plenty of dynamic objects are present during data collection, approximately 60 s of no satellite reception occurred. Positioning and velocity determination were not performed in this period. The ground truth is provided by the highprecision integrated navigation. More information can be seen at reference.<sup>56</sup>.

Fig. 15 indicates the horizontal and vertical  $v_E$  with different methods. From the figure, the  $v_E$  of the GS-LASSO in the deep urban environment are always the lowest. The RMSE values of the eastern and the northern  $v_E$  are below 0.60 m/s, with the upward  $v_E$  being below 1 m/s. It should be emphasized that the main source of the 3D  $v_E$  reaching m/s-level is the error in the upward components. GS-LASSO can help determine the velocity in the horizontal direction with an accuracy in the order of dm/s. It is thus promising for real-time vehiclemounted applications. However, the  $v_E$  obtained through

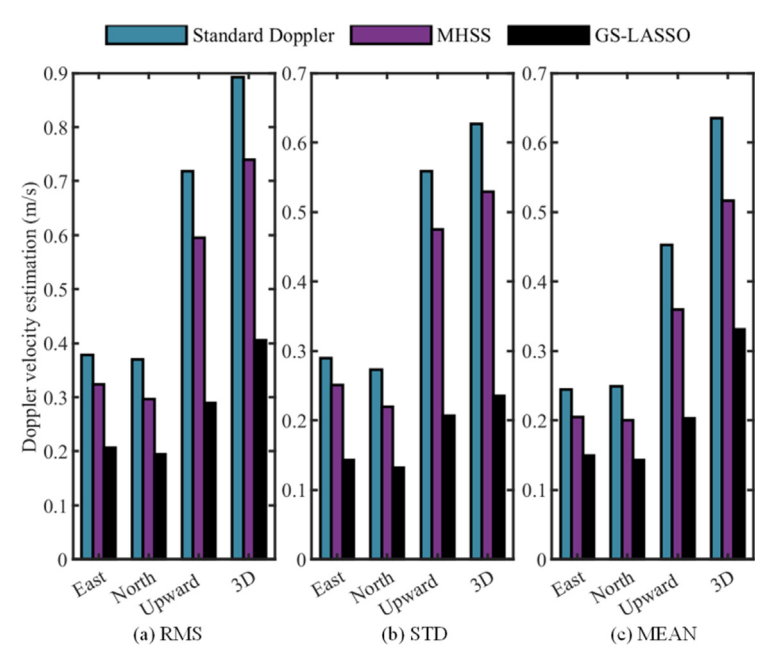


Fig. 13 Statistical information on  $v_E$  including the RMS, STD and Mean value.

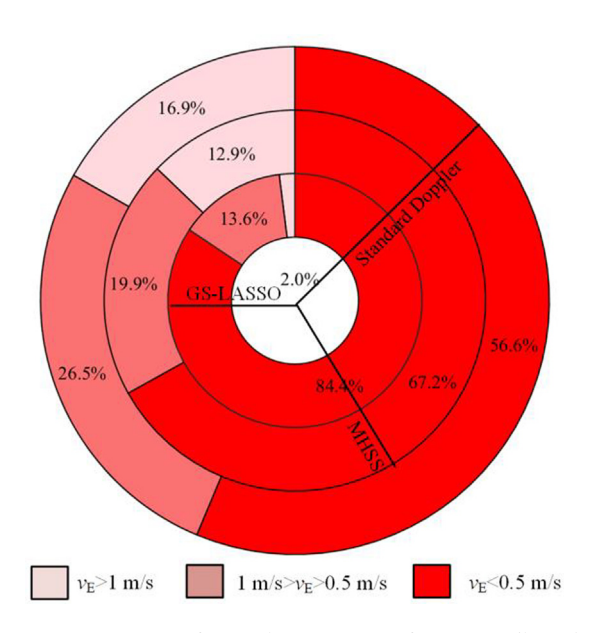


Fig. 14 Percentage for various ranges of  $v_E$  regarding three methods.

MHSS is a little worse than that from the standard Doppler. This may be attributed to the excessive multipath-affected satellites in deep urban environments compared to typical urban settings. Hence, the accuracy of the MHSS detection cannot be ensured, resulting in continued false or missed exclusions. This suggests that further optimization is required when applying MHSS for Doppler velocity determination in urban canyon cases.

Table 2	Computational time comparison of methods.					
$n_{\mathrm{fault}}$	Normalized computation	Normalized computation time				
	GS-LASSO	MHSS				
2	47	74				
3		341				
4		1312				

Table 3 summarizes the percentages across various ranges of 3D- $\nu_{\rm E}$ . The case where  $\nu_{\rm E} < 1$  m/s for GS-LASSO accounts for around 80% of the epochs, significantly outperforming both MHSS and Standard Doppler. After GS-LASSO optimization,  $\nu_{\rm E}$  can remain below 1 m/s in the majority of deep urban environments. In addition, the percentages for the GS-LASSO remain relatively lower than other methods when  $\nu_{\rm E} > 1$  m/s, indicating GS-LASSO strong performance in minimizing  $\nu_{\rm E}$  in this test.

#### 5.3. Experiment in open-sky/suburban environment

In our past two experiments, we primarily examine situations where the satellites used for vehicle positioning experience significant multipath pollution. Here, the cases where the vehicle is not substantially obstructed by buildings are focused on. We use the dataset named CPT collected in the campus, <sup>55</sup> mainly containing open-sky and suburban environments to assess the algorithm performance. Dynamic field data was collected using a Trimble R10 receiver mounted on a tricycle on March 28, 2019 in the Nanhu Campus of China University of Mining and Technology. The test lasted for 2 300 s, with the vehicle remaining stationary for the first 600 s before transitioning

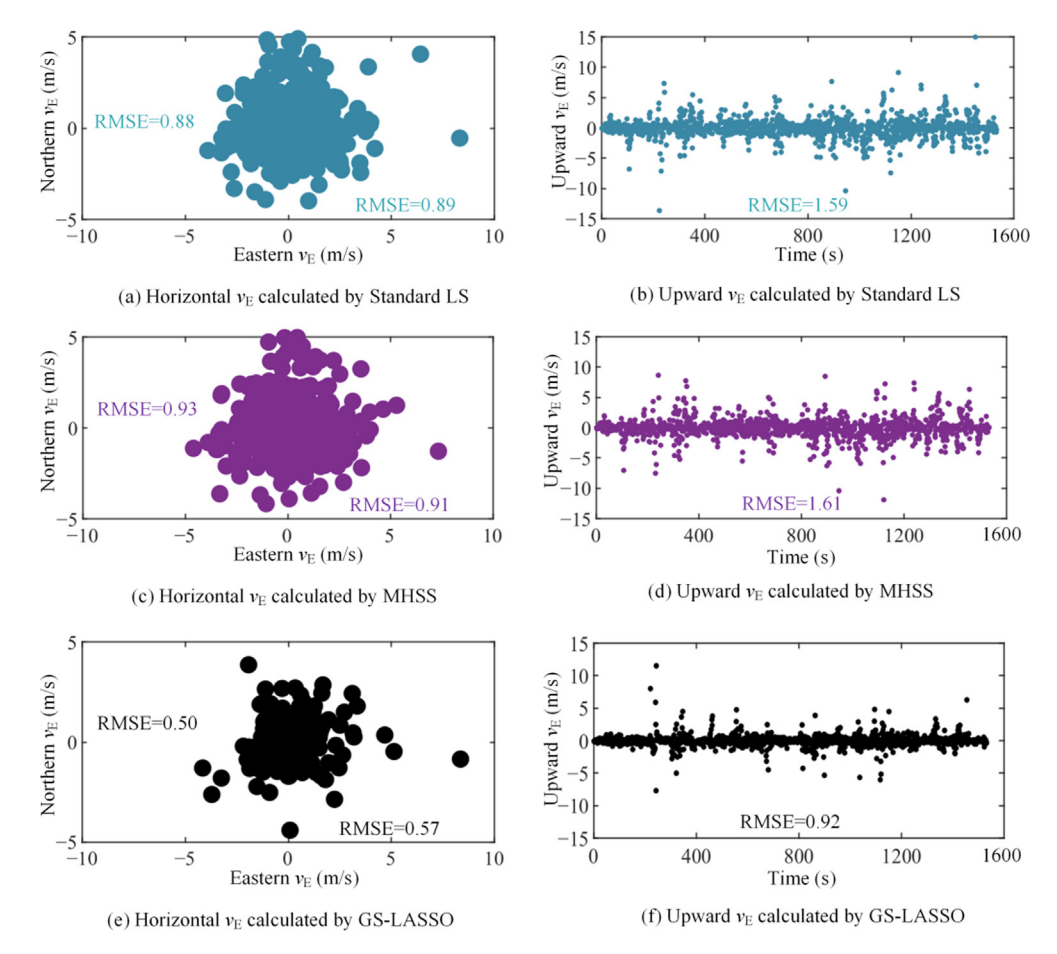


Fig. 15 Horizontal and upward  $v_{\rm F}$  for three methods. The figure also provides corresponding RMSE.

<b>Table 3</b> Sample numbers of different ranges of $v_E$ .							
Velocity error (cm/s)	Standard Doppler	MHSS	GS-LASSO				
$v_{\rm E} > 500$	40	53	15				
$500 > v_{\rm E} > 200$	305	296	83				
$200 > v_{\rm E} > 100$	349	374	188				
$100 > v_{\rm E}$	781	752	1 189				

into driving mode. Throughout the test, the tricycle was only slightly affected by trees and buildings, ensuring high-quality GNSS observations. Doppler measurements from multiple constellations will be used for velocity determination, including GPS, GAL and BDS. The ground truth value is provided by the high-precision integrated navigation. More information can be seen at reference.<sup>55</sup>

We focus on the time series of three-dimensional velocity errors. Fig. 16 presents the time series of the  $v_{\rm E}$  with time. When the vehicle is stationary in an open-sky environment, the velocity error is small. RMSE provided by the three methods are below 0.03 m/s, respectively. As the vehicle begins to be dynamic, the  $v_{\rm E}$  increases due to thermal noise. RMSE provided by the three methods are 0.28, 0.23, and 0.21 m/s, respectively. In the whole test, the RMSE of the standard Doppler method is 0.24 m/s, while the RMSE of MHSS and GS-LASSO are 0.20 m/s and 0.17 m/s, respectively. Our exam-

ination reveals that the standard Doppler still results in the most significant  $\nu_{\rm E}$ . The estimation by GS-LASSO demonstrates diminished error impacts after eliminating the potential outliers.

We finally compare the computational load in this case. Our results indicate that in open environments, the computational time for MHSS is roughly three times that of GS-LASSO. This is because the chi-square statistic employed in MHSS swiftly identifies satellites affected by multipath contamination, thereby enabling MHSS practical. Consequently, MHSS requires fewer computational resources than those in the urban environments.

#### 6. Conclusions and perspectives

This paper examines the optimization of Doppler-based velocity estimation for standalone receivers in urban areas through FDC. The GS-LASSO was proposed by assuming multipath/NLOS groupings and sparsity. Grouping constraints were established using the sky-map and C/N<sub>0</sub>. A non-convex arctangent cost was introduced to encourage sparsity and mitigate multipath/NLOS outliers. An efficient solution for GS-LASSO was proposed using the ADMM solver, with the fixed-point method accounting for the non-convexity of the arctangent cost. Parameter tuning was facilitated by integrating GS-LASSO with the false alarm probability bound. Our method could significantly reduce velocity errors. In Shanghai, the typ-

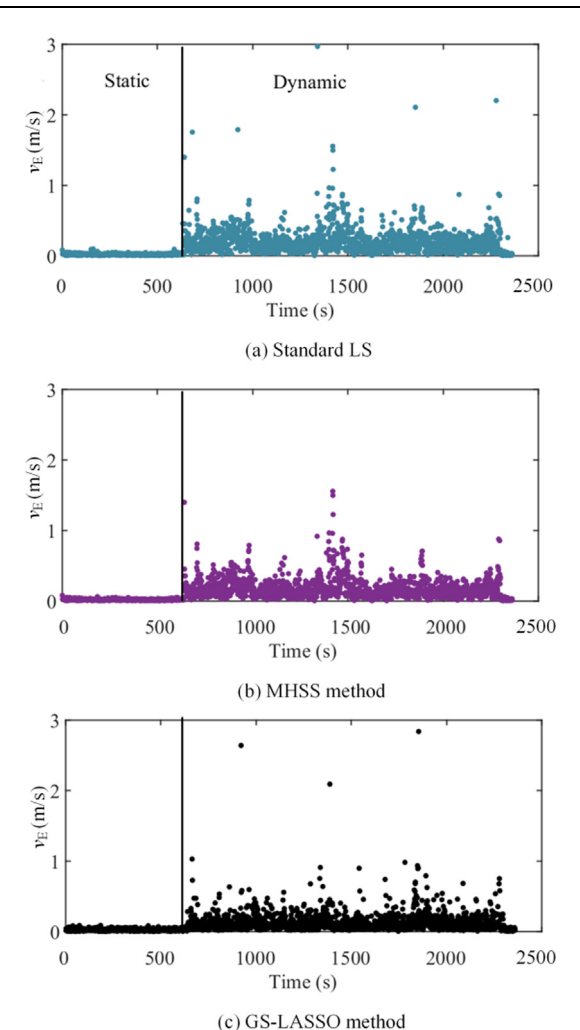


Fig. 16 Time series of  $3D-v_E$  in CPT test.

ical urban area, where exclusion cannot be ensured by MHSS, GS-LASSO provided errors reduced by 35% with only 14% of the computational load.

In future, the following three points should be noted. First, we hope to try combining multi-source sensors such as fisheye cameras or LiDAR with GS-LASSO to provide a more accurate grouping solution. Second, integrity risk, as an important metric for navigation systems, is not considered in this study. Future research will incorporate integrity analysis. Third, it is assumed the multipath/NLOS-affected satellites within a group are dense, meaning that multipath/NLOS in one satellite implies that other satellites in the group are also affected by multipath/NLOS. In the future, this constraint will be relaxed to allow for sparsity of multipath/NLOS-affected satellites both within and between groups.

#### CRediT authorship contribution statement

**Zhen GAO:** Writing – original draft, Visualization, Validation, Software, Methodology, Investigation, Formal analysis. **Rong YANG:** Writing – review & editing, Resources, Project administration, Funding acquisition, Data curation. **Xingqun ZHAN:** Writing – review & editing, Supervision, Project administration. **Yiping JIANG:** Writing – review & editing.

#### Declaration of competing interest

The authors declare that they have no known competing financial interests or personal relationships that could have appeared to influence the work reported in this paper.

#### Acknowledgement

This work was supported by the National Key R&D Program of China (No. 2022YFB3904401).

## Appendix A. Analysis of the Impact of NLOS and multipath on Doppler shifts

For NLOS signals, the NLOS effect is related to receiver motion's impact. In the absence of NLOS, Doppler shift  $f_{rLOS}$  can be shown as 15

$$f_{\text{r,LOS}}^{j} = \frac{|\dot{r}_{\text{r}}|_{2} \cos\left(\theta_{\text{s,LOS}}^{j}\right) \cos\left(\varphi_{\text{s,LOS}}^{j} - \varphi_{\text{r}}\right)}{\lambda_{j}} \tag{A1}$$

where  $|\dot{r}_{\rm r}|_2$  is the velocity amplitude.  $\theta_{\rm s,LOS}^j$  and  $\varphi_{\rm s,LOS}^j$  is the elevation angle and azimuth angle of the *j*th direct signals.  $\varphi_{\rm r}$  is the user heading. For NLOS satellites, assuming the reflection is specular, namely the elevation angle remains the same before and after reflection, the user's Doppler shift reading <sup>15</sup>

$$\dot{f_{\rm r,LOS}}^j = \frac{|\dot{r_{\rm r}}|_2 \cos\left(\theta_{\rm s,LOS}^j\right) \cos\left(\varphi_{\rm s,NLOS}^j - \varphi_{\rm r}\right)}{\lambda_j} \tag{A2}$$

where  $\varphi_{s,NLOS}^j$  is the azimuth angle of *j*th reflected signal. The sole distinction between Eqs. (A1) and (A2) lies in the azimuth angle, which is related with the geometric configuration of the reflecting point and the satellite. In theory, given a known reflecting point,  $\varphi_{s,NLOS}^j$  can be uniquely ascertained. When additional data are available, such as a three-dimensional city model, <sup>15</sup> the NLOS Doppler error can be directly discerned. Nonetheless, for an individual GNSS user, this information is inaccessible, rendering unknown. Yet, the amplitude of the Doppler error induced by NLOS adheres to

$$\begin{aligned} \left| \Delta f_{\mathrm{r,NLOS}}^{j} \right| &= \left| f_{\mathrm{r,NLOS}}^{j} - f_{\mathrm{r,NLOS}}^{j} \right| \\ &= 2 \left| \dot{\mathbf{r}}_{\mathrm{r}} \right|_{2} \cos \left( \theta_{\mathrm{s,LOS}}^{j} \right) \left| \sin \left( \varphi_{\mathrm{s,LOS}}^{j} / 2 + \varphi_{\mathrm{s,NLOS}}^{j} / 2 - \varphi_{\mathrm{r}} \right) \right| \\ &\times \sin \left( \varphi_{\mathrm{s,NLOS}}^{j} / 2 - \varphi_{\mathrm{s,LOS}}^{j} / 2 \right) \left| / \lambda_{j} \right| \end{aligned} \tag{A3}$$

This indicates that the amplitude of the Doppler error can be bounded by  $2|\dot{\mathbf{r}}_{\rm r}|_2 \cos\left(\theta_{\rm s,LOS}^j\right)/\lambda_j$ . When the user moves along a street and parallel to building point, i.e.  $\varphi_{\rm s,LOS}^j/2+\varphi_{\rm s,NLOS}^j/2-\varphi_{\rm r}$  approaches zero,  $|\Delta f_{\rm r,NLOS}^j|$  is much smaller than the upper limit  $2|\dot{\mathbf{r}}_{\rm r}|_2 \cos\left(\theta_{\rm s,LOS}^j\right)/\lambda_j$ . In other words, this inequality is conservative.

Unlike NLOS, the case involving multipath is significantly more complex. In multipath scenarios, the receiver simultaneously receives both direct and reflected signals. Consequently, even with knowledge of the reflecting points, it is challenging to detect the direction of the multipath. The Doppler frequency error  $\Delta f_{\rm r,MP}^j$  caused by multipath can be described as <sup>29</sup>

$$\Delta f_{\text{r,MP}}^{j} = f_{\text{r,MP}}^{j} - f_{\text{r,LOS}}^{j} \approx \left(\dot{\mathbf{r}}_{r} \cdot \mathbf{e}_{\text{mp}}^{j} - \dot{\mathbf{r}}_{r} \cdot \mathbf{e}_{\text{LOS}}^{j}\right) / \lambda_{j} \tag{A4}$$

where  $e_{\rm mp}^{j}$  means the unit vector from the jth satellite pointing toward the direction of the strongest signal, which cannot be measured in practice.  $f_{\rm r,MP}^{j}$  and  $f_{\rm r,LOS}^{j}$  are the Doppler shifts in the multipath and nominal case, respectively.  $e_{\rm LOS}^{j}$  means the unit vector from the jth satellite pointing toward the direct signal. But we have the following inequality  $^{29}$ 

$$(\dot{\mathbf{r}}_r \cdot \mathbf{e}_{LOS}^j - |\mathbf{r}_r|)/\lambda_i \leqslant \Delta f_{rMP}^j \leqslant (\dot{\mathbf{r}}_r \cdot \mathbf{e}_{LOS}^j + |\mathbf{r}_r|)/\lambda_i \tag{A5}$$

This implies that the Doppler outliers caused by multipath can also be bounded by velocity and the LOS elevation angle. According to the work,<sup>29</sup> in practical experiments,  $\Delta f_{r,MP}^{j}$  is also significantly smaller than bounds given in Eq. (A5).

In summary, through the analysis of the impact of existing NLOS and multipath on Doppler observations, it can be observed that both affect the Doppler shift of the receiver. The difference between them lies in the fact that when prior information (such as 3D maps) is known, the Doppler error described in Eq. (A3) can be accurately estimated, whereas the error caused by multipath Eq. (A4) cannot be determined due to the inability to identify the direction of multipath signals, even when the reflecting point information is known. The similarities between them are as follows: First, both Doppler errors can be modeled as the additive. Second, when using only GNSS measurements without external information, the directions of NLOS and multipath signals are both unknown. Consequently, some related optimization methods in the measurement domain do not differentiate between the impacts of NLOS and multipath on Doppler errors. 17,19 We have adopted this approach as well. More precise analysis will be conducted in future.

Upon further analysis, it becomes evident that the upper bound of the additive Doppler error is constrained by variables associated with velocity, and given the limited velocity of vehicles in urban environments, this upper bound is consequently smaller than the Doppler observations recorded at the satellite end. As a result, the variation in Doppler error attributable to the accuracy of velocity estimation is constrained. Taking into account the coupling between velocity estimation and the unknown directions of NLOS/multipath signals, for the sake of estimation simplicity, we model Doppler outliers as an additive fault that is independent of velocity.

#### Appendix B. Convergence analysis of ADMM solver

The convergence of the ADMM solver can be analyzed under the framework proposed by Eckstein & Bertsekas. 46 Consider  $\frac{1}{2}(\textbf{\textit{W}}(\textbf{\textit{Z}}-\textbf{\textit{f}}))^{\text{T}}(\textbf{\textit{W}}(\textbf{\textit{Z}}-\textbf{\textit{f}})) + \lambda \sum_{i=1}^{B} \sqrt{m_i} \psi(|\textbf{\textit{f}}_i|_2, a)$  is closed, proper, convex function. Consider arbitrary  $\eta > 0$ , vector  $\textbf{\textit{u}}^0 \in \mathbb{R}^n$  and  $\textbf{\textit{z}}^0 \in \mathbb{R}^n$ . Suppose  $\{a^k \geq 0, k = 0, 1, \cdots, \infty\}$  and  $\{b^k \geq 0, k = 0, 1, \cdots, \infty\}$  are two sequences which are absolutely summable, such that  $\sum_{k=0}^{\infty} a^k < \infty$  and  $\sum_{k=0}^{\infty} b^k < \infty$ . Consider three sequences  $\{\textbf{\textit{f}}^k \in \mathbb{R}^n, k = 0, 1, \cdots\}$ ,  $\{\textbf{\textit{u}}^k \in \mathbb{R}^n, k = 0, 1, \cdots\}$  and  $\{\textbf{\textit{z}}^k \in \mathbb{R}^n, k = 0, 1, \cdots\}$  satisfying

$$a^{k} \geqslant \left| f^{k+1} - \arg \min_{f} \left\{ \lambda \sum_{i=1}^{B} \sqrt{m_{i}} \psi(|f_{i}|_{2}, a) - (z^{k})^{\mathsf{T}} (\mathbf{W}f + \mathbf{u}^{k} - \mathbf{W}\mathbf{Z}) + \frac{\eta}{2} |\mathbf{W}f + \mathbf{u}^{k} - \mathbf{W}\mathbf{Z}|_{2}^{2} \right\} \right|$$
(B1)

$$b^{k} \geqslant \left| \boldsymbol{u}^{k+1} - arg \min_{\boldsymbol{u}} \left\{ \frac{1}{2} \boldsymbol{u}^{\mathsf{T}} \boldsymbol{u} - \left( z^{k} \right)^{\mathsf{T}} \left( \boldsymbol{W} f^{k+1} + \boldsymbol{u} - \boldsymbol{W} \boldsymbol{Z} \right) + \frac{\eta}{2} \left| \boldsymbol{W} f^{k+1} + \boldsymbol{u} - \boldsymbol{W} \boldsymbol{Z} \right|_{2}^{2} \right\} \right|$$
(B2)

$$z^{k+1} = z^k - \eta (W f^{k+1} + u^{k+1} - W Z)$$
 (B3)

The theorem lies on the fact if there is a solution for Eq. (17), the sequence  $\{f^k\}$  converges to the unique underlying solution. On the contrary, if there is no solution for Eq. (17), then at least one of the sequences  $\{u^k\}$  or  $\{z^k\}$  diverges.

This theorem sheds light on the fact that if the subproblems Eq. (23) and Eq. (31) has the exact solution, namely the summary of error sequence is finite, convergence is ensured. For Eq. (23), although  $\psi(|f_i|_2, a)$  is non-convex, its exact solution can still be ensured. Although a proximal term has been introduced in Eq. (24), it can be strictly proven that such a proximal term does not cause accuracy degradation. Therefore, the accuracy of the ADMM can be guaranteed. Besides, the convergence of the fixed-point iteration is also helpful to ensure solution of ADMM is exact. For Eq. (31), a closed-form of solution is presented. Therefore, the convergence of the ADMM solver can be guaranteed and the sequences of ADMM converge to their optimal points.

#### Appendix C. CDF of weighted chi-square distribution

The goal of this subsection is to delineate the CDF of the of the weighted chi-square distribution. Suppose a random variable S can be seen as the weighted sum of K random variables  $X_i$  ( $1 \le i \le K$ ) following standard chi-square distribution as follows

$$S = \alpha_1 X_1 + \alpha_1 X_2 + \dots + \alpha_K X_K \tag{C1}$$

where  $\alpha_i$  is the input weight. The DOF of the  $X_i$  is  $v_i$ . The distribution of S can be simplified as CDF(s) =  $h(s, \alpha, \mathbf{DOF})$ , where  $\alpha$  covering all  $\alpha_i$  and **DOF** is a vector covering all  $v_i$ . The specific distribution is given as follows.<sup>54</sup>

Supposing *s* is the argument, the CDF of the weighted chisquare distribution can be obtained as

$$CDF(s) = \frac{e^{-s/(2\beta)}}{(2\beta)^{\nu/2+1}} \cdot \frac{s^{\nu/2}}{\Gamma(\nu/2+1)}$$

$$\sum_{k \ge 0} \frac{k! \xi_k}{(\nu/2+1)_k} \mathcal{L}_k^{(\nu/2)} \left(\frac{(\nu+2)s}{4\beta\mu_0}\right)$$
(C2)

where  $\beta$  is a transformed coefficient to simplify the formula.  $\nu$  is the sum of the DOF covering all groups.  $\Gamma(\cdot)$  is the Gamma function.  $\mu_0$  is a positive coefficient related with  $\nu$ .  $\mathcal{L}_k^{\nu/2-1}(\cdot)$  is the kth generalized Laguerre polynomial.  $\xi_k$  are the coefficients, reading as

$$\xi_k = \frac{1}{k} \sum_{i=0}^{k-1} \xi_j d_{k-j}, k \ge 1$$
 (C3)

$$\xi_0 = \left(\frac{q}{\mu_0}\right)^{\nu/2} \frac{2\beta q}{q - \mu_0} \prod_{i=1}^K \left(1 + \frac{\alpha_i (q - \mu_0)}{\beta \mu_0}\right)^{-\nu/2} \tag{C4}$$

$$d_{j} = \left(\frac{-\mu_{0}}{q - \mu_{0}}\right)^{j} + \frac{1}{2} \sum_{i=1}^{K} v_{i} \left(\frac{\mu_{0}(\beta - \alpha_{i})}{\beta \mu_{0} + \alpha_{i}(q - \mu_{0})}\right)^{j}, j \geqslant 1$$
 (C5)

where q = v/2 + 1 is the convolution parameter.

#### References

- Hu S, Zhao HB, Zhuang C. A whole-net cooperative positioning method based on CDGNSS and inter-vehicle ranging. *Chin J Aeronaut* 2024;37(2):401–16.
- Xue KY, Shi C, Wang C. ATS-UNet: Attentional 2-D time sequence UNet for global ionospheric one-day-ahead prediction. *IEEE Geosci Remote Sens Lett* 2024;21:1002505.
- 3. Schmidt GT. Navigation sensors and systems in GNSS degraded and denied environments. *Chin J Aeronaut* 2015;**28**(1):1–10.
- 4. Jeong H, Kee C, Song J, et al. Integrity monitoring for urban air mobility using time-differenced carrier phase. *The international technical meeting of the the institute of navigation*, 2023.
- Liu WK, Shi X, Zhu F, et al. Quality analysis of multi-GNSS raw observations and a velocity-aided positioning approach based on smartphones. Adv Space Res 2019;63(8):2358–77.
- Hu J, Liu WK, Zhu F, et al. V-RTK: a velocity-constrained RTK algorithm to improve position accuracy of low-cost receiver in urban environments. Adv Space Res 2023;72 (11):4721–34.
- Liu F, Balazadegan Sarvrood Y, Liu Y, et al. Stereo visual odometry with velocity constraint for ground vehicle applications. J Navig 2021;74(5):1026–38.
- Chi C, Zhang X, Liu JH, et al. GICI-LIB: A GNSS/INS/camera integrated navigation library. *IEEE Robot Autom Lett* 2023;8 (12):7970-7.
- Ji L, Sun R, Cheng Q, et al. Evaluation of the performance of GNSS-based velocity estimation algorithms. Satell Navig 2022;3 (1):18.
- Wang XX, Tu R, Gao YP, et al. Velocity estimations by combining time-differenced GPS and Doppler observations. *Meas Sci Technol* 2019;30(12):125003.
- Zhang LH, Chang GB, Chen C, et al. GNSS velocimeter by adaptively combining carrier phase and Doppler measurements. *IET Sci Meas Technol* 2020;14(7):762–71.
- 12. Wang XX, Tu R, Zhang R, et al. A study of GPS PPP velocity estimation with the constraints of Doppler observation. *Adv Space Res* 2020;66(12):2900–13.
- Chang GB, Qian NJ, Chen C, et al. Precise instantaneous velocimetry and accelerometry with a stand-alone GNSS receiver based on sparse kernel learning. *Measurement* 2020;159:107803.
- 14. Qian NJ, Chang GB, Gao JX, et al. Vehicle's instantaneous velocity reconstruction by combining GNSS Doppler and carrier phase measurements through Tikhonov regularized kernel learning. *IEEE Trans Veh Technol* 2021;70(5):4190–202.
- Zhang LY, Ng HF, Zhang GH, et al. Ray-tracing correction for GNSS velocity estimation using Doppler frequency: a feasibility analysis. IEEE Trans Instrum Meas 2024;73:8503210.
- 16. Kulemann D, Schön S. Towards integrity monitoring of GNSS velocity estimates in urban environment. *ION GNSS+*, the international technical meeting of the satellite division of the institute of navigation, 2023.
- 17. Guo J, Fan ZY, Li Z, et al. Doppler velocity estimation based on the random sample consensus considering a prior dynamic model. *Adv Space Res* 2025;**75**(4):3471–85.
- 18. Brizzi M, Neri A, Rispoli F. A solution separation algorithm for velocity estimation in rail and road applications. ION GNSS+, the international technical meeting of the satellite division of the institute of navigation, 2023.
- Gao YT, Jiang Y, Liu BY, et al. Integrity monitoring of multiconstellation GNSS-based precise velocity determination in urban environments. *Measurement* 2023;222:113676.
- Lesouple J, Robert T, Sahmoudi M, et al. Multipath mitigation for GNSS positioning in an urban environment using sparse estimation. *IEEE Trans Intell Transp Syst* 2019;20(4):1316–28.
- 21. Zhang P, Li DA, Zhao JM, et al. Multipath mitigation in GNSS positioning by the dual-path compression estimation. *IEEE Sens J* 2020;**20**(6):3087–100.

22. Yuan Y, Shen F, Xu DJ. Multipath modeling and mitigation by using sparse estimation in global navigation satellite system-challenged urban vehicular environments. *Int J Adv Rob Syst* 2020;17(5):1729881420968696.

- 23. Wang SZ, Zhan XQ, Zhai YW, et al. Highly reliable relative navigation for multi-UAV formation flight in urban environments. *Chin J Aeronaut* 2021;34(7):257–70.
- 24. Yuan HJ, Zhang ZT, He XF, et al. Multipath mitigation in GNSS precise point positioning using multipath hierarchy for changing environments. *GPS Solut* 2023;27(4):193.
- 25. Tibshirani R. Regression shrinkage and selection via the lasso. *J R Stat Soc Ser B Methodol* 1996;**58**(1):267–88.
- Schmidt E, Gatsis N, Akopian D. A GPS spoofing detection and classification correlator-based technique using the LASSO. *IEEE Trans Aerosp Electron Syst* 2020;56(6):4224–37.
- Yuan Y, Shen F, Li XD. GPS multipath and NLOS mitigation for relative positioning in urban environments. *Aerosp Sci Technol* 2020;107:106315.
- 28. Qi HT, Cui XW, Lu MQ. Fast exclusion candidate identification based on sparse estimation for ARAIM fault exclusion process. *Remote Sens* 2024;16(18):3537.
- 29. Xie P, Petovello MG. Measuring GNSS multipath distributions in urban canyon environments. *IEEE Trans Instrum Meas* 2015;**64**(2):366–77.
- **30.** Cheng Q, Sun R, Wang JH. Analysis of multipath effects on velocity measurement from GPS Doppler observations. *J Beijing Univ Aeronaut Astronaut* 2021;**47**(9):1807–13 [Chinese].
- Hewitson S, Wang JL. GNSS receiver autonomous integrity monitoring (RAIM) performance analysis. GPS Solut 2006;10 (3):155-70.
- Berk A, Brugiapaglia S, Hoheisel T. LASSO reloaded: a variational analysis perspective with applications to compressed sensing. SIAM J Math Data Sci 2023;5(4):1102–29.
- 33. Yan ZB, Yao Y. Variable selection method for fault isolation using least absolute shrinkage and selection operator (LASSO). *Chemom Intell Lab Syst* 2015;**146**:136–46.
- 34. Zhang ZW, Huang WG, Liao Y, et al. Bearing fault diagnosis via generalized logarithm sparse regularization. *Mech Syst Signal Process* 2022;**167**:108576.
- 35. Yuan M, Lin Y. Model selection and estimation in regression with grouped variables. *J R Stat Soc Ser B Stat Methodol* 2006;**68**(1):49–67.
- 36. Chen PY, Selesnick IW. Group-sparse signal denoising: Non-convex regularization, convex optimization. *IEEE Trans Signal Process* 2014;**62**(13):3464–78.
- 37. Liu JJ, Qiao BJ, Wang YN, et al. Non-convex sparse regularization via convex optimization for impact force identification. *Mech Syst Signal Process* 2023;**191**:110191.
- 38. Li ZP, Qiao BJ, Wen B, et al. Time analysis for aero-engine acoustic modes exploiting block sparsity. *Chin J Aeronaut* 2024;37(11):254–64.
- 39. Sánchez JS, Gerhmann A, Thevenon P, et al. Use of a FishEye camera for GNSS NLOS exclusion and characterization in urban environments. *The international technical meeting of the the institute of navigation*, 2016.
- **40.** Wen WS, Bai XW, Kan YC, et al. Tightly coupled GNSS/INS integration via factor graph and aided by fish-eye camera. *IEEE Trans Veh Technol* 2019;**68**(11):10651–62.
- Sun R, Hsu LT, Xue DB, et al. GPS signal reception classification using adaptive neuro-fuzzy inference system. J Navigation 2019;72(3):685–701.
- 42. Li LT, Elhajj M, Feng YX, et al. Machine learning based GNSS signal classification and weighting scheme design in the built environment: a comparative experiment. *Satell Navig* 2023;4 (1):12.
- 43. Xu PH, Zhang GH, Yang B, et al. Machine learning in GNSS multipath/NLOS mitigation: Review and benchmark. *IEEE Aerosp Electron Syst Mag* 2024;39(9):26–44.

- Strode PR, Groves PD. GNSS multipath detection using three-frequency signal-to-noise measurements. GPS Solut 2016;20 (3):399–412.
- 45. Pan YL, Xu KD, Wei S, et al. Efficient distributed optimization for large-scale high-dimensional sparse penalized Huber regression. *Commun Stat Simul Comput* 2024;53(7):3106–25.
- Eckstein J, Bertsekas DP. On the Douglas—Rachford splitting method and the proximal point algorithm for maximal monotone operators. *Math Program Ser A B* 1992;55(1– 3):293–318.
- Banach S. Sur les opérations dans les ensembles abstraits et leur application Aux équations intégrales. Fund Math 1922;3:133–81.
- 48. He BS, Yuan XM. On non-ergodic convergence rate of Douglas— Rachford alternating direction method of multipliers. *Numer Math* 2015;130(3):567–77.
- Knowles D, Gao G. Greedy detection and exclusion of multiple faults using euclidean distance matrices. arXiv preprint:2024.12617; 2024.
- Kronvall T, Jakobsson A. Hyperparameter selection for groupsparse regression: A probabilistic approach. *Signal Process* 2018;151:107–18.

- 51. Zou H. The adaptive lasso and its oracle properties. *J Am Stat Assoc* 2006;**101**(476):1418–29.
- 52. Rakotomamonjy A, Flamary R, Salmon J, et al. Convergent working set algorithm for lasso with non-convex sparse regularizers. *Proceedings of the 25th international conference on artificial intelligence and statistics.* 2022. p. 5196–211.
- 53. Yang TY, Sun DF. Global navigation satellite systems fault detection and exclusion: a parameterized quadratic programming approach. *IEEE Trans Aerosp Electron Syst* 2020;56(4):2862–71.
- Castaño-Martínez A, López-Blázquez F. Distribution of a sum of weighted central Chi-square variables. *Commun Stat Theory Meth* 2005;34(3):515–24.
- Chen K, Chang GB, Chen C. GINav: A MATLAB-based software for the data processing and analysis of a GNSS/INS integrated navigation system. GPS Solut 2021;25(3):108.
- 56. Hsu LT, Huang F, Ng HF, et al. Hong Kong UrbanNav: an open-source multisensory dataset for benchmarking urban navigation algorithms. *Navi* 2023;70(4):602.